International Journal of Mechanical Sciences 254 (2023) 108413

Contents lists available at ScienceDirect

International Journal of Mechanical Sciences

journal homepage: www.elsevier.com/locate/ijmecsci

Effect of splitter plate length on FIV of circular cylinder

Enhao Wang [a,*], Sihan Zhao [a], Wanhai Xu [b,*], Qing Xiao [c], Bing Li [a]

[a] Institute for Ocean Engineering, Shenzhen International Graduate School, Tsinghua University, Shenzhen 518055, Guangdong, China
[b] State Key Laboratory of Hydraulic Engineering Simulation and Safety, Tianjin University, Tianjin 300350, China
[c] Department of Naval Architecture, Ocean and Marine Engineering, University of Strathclyde, Glasgow G4 0LZ, Scotland, UK

ARTICLE INFO

Keywords:
Splitter plate
Flow-induced vibration (FIV)
Vortex-induced vibration (VIV)
Galloping
Low Reynolds number

ABSTRACT

The influence of the plate length on the flow-induced vibration (FIV) of a circular cylinder with a rigid splitter plate is numerically studied at a low Reynolds number of 100. The mass and damping ratios of the system are respectively $m^* = 10$ and $\zeta = 0$. The reduced velocity (V_r) is varied from 2 to 26 and seven different nondimensional splitter plate length (L^*) values in the range of 0–2 are considered. Three different response patterns are identified in the present research, namely vortex-induced vibration (VIV), combined VIV-galloping and weak VIV-galloping. When the system is undergoing VIV, the frequency synchronisation is delayed and the lock-in range is enlarged with increasing L^*. The onset of galloping is postponed with the kink alleviated and the galloping frequency lowering. Abrupt drops in the vortex and total phases are associated with the initiation of galloping. In the galloping branch, both vortex and total forces remain in phase with the displacement. For the added mass and excitation coefficients (C_{ay} and C_{ey}) of the cylinder-plate assembly which have rarely been reported in the literature, C_{ay} decreases as V_r is increased in the VIV range. Nevertheless, it leaps at the onset of galloping and the galloping response is accompanied by positive C_{ay} values. C_{ey} is negative in most cases and its trough appears at beginning of the VIV lock-in range or around the kink in the galloping branch. Due to the large-amplitude and low-frequency nature of the galloping oscillation, three new multi-vortex wake patterns (4P, 5P and 6P) are found to take place. Overall, for a longer splitter plate in the present study, the shear layer reattachment is observed at lower V_r and the galloping oscillation is associated with more vortex pairs.

1. Introduction

A splitter plate is a plate attached to a structure so that it splits the wake. It was originally designed as a type of wake stabiliser due to its capability of increasing the base pressure (reducing the drag) as well as eliminating the vortex formation [1]. Extensive studies have been carried out to better understand how a splitter plate influences the flow around a stationary circular cylinder. Apelt and his co-workers [2,3] performed experimental tests in a water tunnel to investigate the flow past a circular cylinder with a rigid splitter plate. The Reynolds number ($Re = U_\infty D/\nu$, where U_∞ is the freestream velocity, D stands for the cylinder diameter and ν denotes the kinematic viscosity of the fluid) ranged from 10^4 to 5×10^4 and the plate length (L) to diameter ratio $L^* = L/D =$ 0–7 was adopted. The drag and vortex shedding frequency were found to decrease progressively with increasing L^* until the drag coefficient became a constant and the vortex shedding was eventually suppressed. Kwon and Choi [4] numerically studied the control of laminar vortex shedding behind a circular cylinder using splitter plates. They reported that once L^* was larger than a critical value, the vortex shedding would completely disappear and this critical L^* was proportional to Re. Anderson and Szewczyk [5] examined the effect of a splitter plate on the near wake of a circular cylinder at subcritical Re between 2700 and 46000 using wind tunnels. It was shown that the shear layer characteristics affected the vortex shedding frequency greatly. The variation of the Strouhal number ($St = f_{st} D/U_\infty$ with f_{st} being the vortex shedding frequency) for $L^* =$ 0–1.75 could be divided into four distinct regions. Moreover, the splitter plate decreased the level of three-dimensionality in the formation region by stabilising the transverse flapping of the shear layers. Deep et al. [6] employed a proper orthogonal decomposition (POD) technique to analyse the wake behind a circular cylinder with a splitter plate at Re = 100, 125 and 150. For all the cases considered, the first six modes contributed to more than 95% of the total enstrophy.

Detached splitter plates have also been employed to reduce the flow-induced forces. Hwang et al. [7] simulated the laminar flow past a circular cylinder with a detached splitter plate. $L^* = 1$ and Re = 30, 100 and 160 were considered. The gap ratio G/D, where G is the distance

* Corresponding authors.
E-mail addresses: enhao.wang@sz.tsinghua.edu.cn (E. Wang), xuwanhai@tju.edu.cn (W. Xu).

https://doi.org/10.1016/j.ijmecsci.2023.108413
Received 4 January 2023; Received in revised form 21 April 2023; Accepted 25 April 2023
Available online 6 May 2023
0020-7403/

Nomenclature

A_y	Vibration amplitude in cross-flow direction
c	Structural damping coefficient
C_{ay}, C_{ey}	Added mass coefficient and excitation coefficient
$C_{o\,\max}$	Maximum Courant number
$\overline{C}_x$, C'_x, C'_y	Mean IL force coefficient, RMS of fluctuating IL force coefficient and RMS of fluctuating CF force coefficient
D	Diameter of circular cylinder
f_1, f_2, f_3	Fine, medium and coarse solutions
f_n, f_{oy}, f_{st}	Natural frequency of cylinder-plate assembly, oscillation frequency and Strouhal frequency
F_{vortex}, $F_{potential}$	Vortex force and potential force
F_x, F_y, F_p	IL hydrodynamic force, CF hydrodynamic force and the predicted vortex-induced force in CF direction
G	Distance between rear base point of cylinder and leading edge of splitter plate
GCI	Grid convergence index
$\mathbf{I}$	Unit tensor
k	Structural stiffness
L, L^*	Splitter plate length and dimensionless splitter plate length
L_f	Vortex formation length
m, m_d, m^*	Structural mass, mass of displaced fluid and mass ratio of cylinder-plate system
n	Number of time step
$\mathbf{n}$, $\mathbf{n}_x$, $\mathbf{n}_y$	Outward-pointing normal vector, IL component of normal vector and CF component of normal vector
N_b, N_c, N_s	Number of elements for background mesh, number of elements for component mesh and total number of samples
p, p_{ref}	Pressure and reference pressure
P	Order of accuracy
r	Grid refinement factor
Re	Reynolds number
St	Strouhal number
t	Time
t_p	Thickness of splitter plate
T_{oy}	Oscillation period of cylinder-plate assembly
$\mathbf{u}$, U_∞	Velocity vector of flow field and freestream velocity
V_r	Reduced velocity
y, $\dot{y}$, $\ddot{y}$	CF displacement, CF velocity and CF acceleration
$y_{\max}$, $y_{\min}$	Maximum CF displacement and minimum CF displacement
β	Real parameter in Newmark-β method
Γ	Surface of cylinder-plate system
γ	Real parameter in Newmark-β method
Δt	Time-step size
ε_{21}, ε_{32}	Difference between the medium and fine solutions and difference between the coarse and medium solutions
ζ	Structural damping ratio
μ	Dynamic viscosity of fluid
ν	Kinematic viscosity of fluid
ρ	Density of fluid
$\boldsymbol{\sigma}_f$	Sum of pressure contributed stress component and viscous contributed stress component
ϕ_{vortex}, ϕ_{total}	Vortex phase and total phase
ω_z	Nondimensional spanwise vorticity

between the rear base point of the cylinder and the leading edge of the splitter plate was changed from 0 to 5. It was discovered that there existed an optimal location of the plate for the maximum reduction of the flow-induced forces. However, beyond the optimal location, the flow-induced forces increased sharply. Similar observations were also reported by Dehkordi and Jafari [8] and Serson et al. [9] in their numerical studies. Akilli et al. [10] conducted water tunnel tests to investigate the flow behaviours around a circular cylinder controlled by a splitter plate placed at various locations downstream the cylinder in shallow water. The results showed that the splitter plate had a substantial effect on the suppression of the vortex shedding for G/D between 0 and 1.75. When $G/D = 2$, the effect of the plate was eliminated. The splitter plates in the aforementioned research were solid which prohibited the communication between the two shear layers through the plates. Cardell [11] presented his experimental work on the effect of a permeable splitter plate on the flow past a circular cylinder. When the permeability was high, the flow in the near wake resembled the no splitter plate case. However, for a low permeability, the near wake was almost disconnected from the vortices formed further downstream.

Previous studies have proven that a free-to-rotate splitter plate could lower the drag and lift forces on the cylinder as well. Cimbala and Garg [12] experimentally investigated the flow in the wake of a freely rotatable cylinder with a splitter plate using a wind tunnel at $Re = 5 \times 10^3$–2×10^4. L^* in the range of 0–5 was considered. The combination of the cylinder and the splitter plate could rotate unrestrictedly about the longitudinal axis of the cylinder. It was found that for the L^* values considered, the splitter plate rotated to some off-axis equilibrium angle rather than aligning itself to the free stream. Cimbala and Chen [13] further analysed the freely rotatable cylinder/splitter plate body in transitional and supercritical Re ranges. The authors noted that for the cases with $L^* > 1$, the splitter plate started to oscillate between the extremes on either side in the transitional Re range. At supercritical Re, the splitter plate with $L^* \leq 2$ was managed to regain a new equilibrium angle, whereas for the cases with $L^* \geq 2.5$, the cylinder/splitter plate body continued to oscillate. Similar bifurcating behaviours were confirmed by the numerical results of Lu et al. [14] at low Re. Gu et al. [15] carried out wind tunnel tests on the flow around a circular cylinder with a splitter plate freely rotatable around the cylinder axis. In their study, $Re = 3 \times 10^4$–6×10^4 and L^* ranged from 0.5 to 6. L^* was crucial in determining the equilibrium angle and longer plates led to smaller angles. The mean drag and the root-mean-square fluctuating lift coefficients were less than those of the corresponding plain cylinder with reduction up to 30% and 90%, respectively. Sudhakar and Vengadesan [16] numerically studied the vortex shedding characteristics and the drag force on a circular cylinder attached with an oscillating splitter plate at $Re = 100$. The results indicated that the vortex shedding could be completely suppressed by a short splitter plate with $L^* = 1$ oscillating at very low frequencies. In contrast, when the plate was stationary, $L^* = 5$ was required to achieve such a suppression.

The vortex shedding suppression and drag reduction capabilities of the splitter plates have promoted their utilisation in suppressing the flow-induced vibration (FIV) of cylindrical structures [17–21].

However, existing research showed that a sufficiently long splitter plate was required in order to suppress the FIV successfully [22–24]. For a small L^*, the oscillation of the cylinder might even be exaggerated and galloping-type response could be induced [25–29]. Stappenbelt [22] experimentally investigated the effect of a splitter plate on the dynamics and kinematics of a circular cylinder free to oscillate in the transverse direction. Re ranged from 1.26×10^4 to 8.4×10^4 and $L^* = 0$–4 was examined over a reduced velocity ($V_r = U_\infty/f_n D$, where f_n is the natural frequency of the system) interval of 3 to 60. The attachment of a rigid splitter plate to an elastically restrained circular cylinder introduced the potential for a galloping-type behaviour. As L^* was increased, there was a smooth transition from pure VIV to galloping response. The mitigation of FIV was not achieved until $L^* \geq 2.8$. Assi et al. [25] conducted experiments on the dynamic response of a circular cylinder with a free-to-rotate short-tail fairing and a splitter plate. Non-rotating short splitter plates gave rise to severe galloping over a considerable range of flow velocities. The particle image velocimetry (PIV) measurements suggested that as V_r was increased, the vortex formation length was reduced and reattachment of the shear layers was achieved, resulting in the galloping instabilities of the system. The transverse galloping of a circular cylinder fitted with solid and slotted splitter plates was studied at Re = 1500–16000 by Assi and Bearman [30]. Different splitter plates with variations in plate length and plate porosity were considered. Solid splitter plates of 0.5 and 1 diameter in length were found to produce severe galloping responses. A slotted plate with porosity ratio of 30% also caused considerable vibration but with a reduced rate of increase with the flow velocity. Galloping mechanism was responsible for extracting energy from the flow and driving the oscillations and the reattachment of the free shear layers on the tip of the plate was the hydrodynamic mechanism driving the excitation. Law and Jaiman [31] studied the FIV of a circular cylinder with a rigid splitter plate at a low Re of 100. The cylinder-plate system had a mass ratio ($m^* = m/m_d$, where m is the structural mass and m_d represents the mass of the displaced fluid) of 2.6 and the damping ratio was $\zeta = 0.001$. Large amplitude galloping response was observed at high V_r. Four oscillation patterns were categorised in the wind tunnel experiment of Liang et al. [26], i.e., VIV, complete interaction of VIV-galloping, combined weak VIV and interaction of VIV and galloping and combined weak VIV and pure galloping. The weak oscillation in VIV could accelerate the stabilisation of galloping when the cylinder was released from rest at a given flow velocity. Sun et al. [28] simulated the FIV of an elastically supported cylinder-plate assembly with $L^* = 0$–1.5 at $Re = 100$. As L^* was increased, three FIV modes were observed successively: VIV, coupled VIV and galloping and separated VIV and galloping. The lift components generated from the splitter plate and the cylinder acted as the driving and suppressing forces of galloping, respectively. Sun et al. [24] presented a comprehensive experimental campaign on the transition of FIV for a circular cylinder with splitter plates. In the range of L^* investigated, five oscillation patterns were identified sequentially: VIV, combined VIV-galloping, separated weak VIV (WVIV)-galloping, WVIV and weak galloping and WVIV and desynchronisation. The oscillation could be well suppressed when $L^* > 3.2$. The transition from VIV to galloping was the competition of vortex shedding and reattachment of the free shear layers. Harmonic force component at three times the oscillation frequency was associated with the galloping dominated region of L^* = 0.4–1.8. Sun et al. [1] experimentally investigated the FIV of a cylinder with an upstream rigid splitter plate (USP), a downstream plate (DSP) and symmetrically arranged splitter plates in the Re range of 1100–7700 with L^* = 0–3.6. It was found that both USP and DSP could mitigate the oscillation and reduce the drag. Whereas, significant galloping oscillation was observed for DSP with $L^* = 0.4$–3.2. Weak galloping was excited with the combination of USP and DSP and L^* = 1–1.8. Cui et al. [32] conducted experimental tests to study the control of FIV of a circular cylinder with rigid and flexible splitter plates. Re in their experiment ranged from 1680 to 8720. With a rigid splitter plate, both VIV and galloping were observed. Although the amplitude in the lock-in range was reduced, it increased linearly at high V_r.

According to the literature review above, there have been a number of experimental and numerical studies on the FIV of a circular cylinder with a rigid splitter plate. However, existing research is mostly focused on the response features. Details about the hydrodynamic coefficients especially the added mass and excitation coefficients for such a system have rarely been reported. Moreover, the multi-vortex wake patterns associated with the galloping oscillation have not been properly addressed. In this paper, the FIV of an elastically mounted circular cylinder fitted with rigid splitter plates of different L^* values is numerically investigated at $Re = 100$. The cylinder-plate system has a mass ratio of 10. L^* ranging from 0 to 2 is adopted to evaluate its effect on the FIV characteristics. Besides systematically studying the dynamic responses, particular attention is paid to the hydrodynamic coefficients and vortex shedding modes to unveil the underlying fluid–structure interaction (FSI) mechanisms. The rest of the paper are organised as follows: The numerical method utilised in the present study is detailed in Section 2. A description of the problem investigated is provided in Section 3. The simulation results are presented with in-depth discussion in Section 4. Finally, the main conclusions of this paper are summarised in Section 5.

2. Numerical method

In this section, details about the flow model, the structural dynamic model and the fluid–structure interaction strategy employed in the present numerical simulation are provided.

2.1. Flow model

The governing equations in the fluid domain are the two-dimensional (2D) unsteady incompressible Navier–Stokes (N–S) equations formulated as

$$\nabla \cdot \mathbf{u} = 0 \tag{1}$$

$$\frac{\partial \mathbf{u}}{\partial t} + \nabla \cdot (\mathbf{u}\mathbf{u}) = -\frac{1}{\rho}\nabla p + \nu \nabla^2 \mathbf{u} \tag{2}$$

where $\mathbf{u}$ stands for the velocity vector of the flow field, t denotes the time, ρ is the fluid density, p represents the pressure and ν is the kinematic viscosity of the fluid.

The open source computational fluid dynamics (CFD) toolbox OpenFOAM is adopted to simulate the flow field. A finite volume method (FVM) is used for the discretisation of the N–S equations. The transient term is discretised with a second-order implicit backward scheme, while a second-order upwind scheme is used for the convective terms. The pressure-velocity coupling is solved by the pressure-implicit with splitting of operators (PISO) algorithm [33] in a segregated manner. The overset (also known as Chimera) mesh method is employed to handle the dynamic mesh. It is advantageous to deal with problems involving large displacements and/or relative motion of multiple bodies without compromising the mesh quality which may be degraded by the excessive deformation in the mesh morphing method. For the overset mesh technique, a background grid is firstly generated to discretise the whole computational domain without considering any solid body. Then, each object of interest is wrapped with a body-fitted mesh as a component mesh and overlaps with the background and/or other component meshes. As demonstrated in Fig. 1, cells are classified into the fringe cells which need interpolation from other meshes, field cells which are involved in solving the N–S equations and hole cells that are located inside the solid bodies. A distance based implicit method aided by a regular voxel mesh is employed to quickly cut out the hole. Detailed description of this hole cutting method can be found in Chan and Pandya [34],Druyor [35] and Chen et al. [36]. In order to obtain the solution in the whole computational domain, exchange

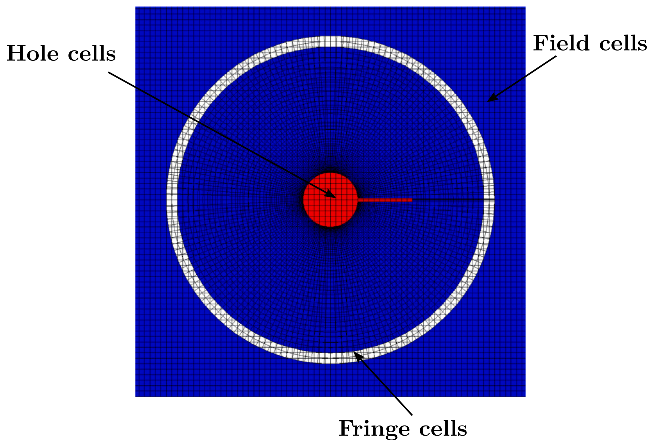

Fig. 1. Different cell types in the overset mesh technique. The colours correspond to: blue—field cells involved in solving the Navier–Stokes equations, white—fringe cells exchanging information with other meshes through interpolation and red—hole cells located inside the solid body.

of the flow information between the different meshes is crucial besides the aforementioned overset mesh assembly. This is realised by using the fringes and donors. A fringe point/cell, also named a receptor, receives the solution information from its donors on the sibling meshes. Interpolations of the flow variables of the donors are performed to obtain those at the receptor. In the present simulation, a distance weighted function is adopted for the information exchange.

2.2. Structural dynamic model

The 1DOF FIV of a circular cylinder with a rigid splitter plate in the transverse direction can be described by

$$m\ddot{y} + c\dot{y} + ky = F_y \tag{3}$$

where m, c and k are respectively the structural mass, damping coefficient and stiffness, y is the cross-flow (CF) displacement of the cylinder-plate assembly, a dot denotes differentiation with respect to time and F_y is the hydrodynamic force in the transverse direction.

The implicit Newmark-β method with a second-order accuracy as detailed in Newmark [37] is used to integrate the equation of motion. This method relates the displacement, velocity and acceleration from time step n to $n+1$ in the following way:

$$\dot{y}^{n+1} = \dot{y}^n + \Delta t\left[(1-\gamma)\,\ddot{y}^n + \gamma\,\ddot{y}^{n+1}\right] \tag{4}$$

$$y^{n+1} = y^n + \Delta t\,\dot{y}^n + \frac{\Delta t^2}{2}\left[(1-2\beta)\,\ddot{y}^n + 2\beta\,\ddot{y}^{n+1}\right] \tag{5}$$

here the superscripts represent the time-step numbers, Δt is the time-step size, β and γ are two real parameters concerning the accuracy and stability of the integration method. In this study, $\beta = 1/4$ and $\gamma = 1/2$ are chosen corresponding to the average acceleration method with unconditional stability.

2.3. Fluid–structure interaction

A loosely coupled strategy is adopted in the present FSI simulation, i.e., the flow field and the dynamic response of the structure are solved successively within a given time step. The FSI procedures are briefly summarised as follows: (i) The interpolation stencils are generated for the communication between the different meshes and the N–S equations are solved to compute the hydrodynamic forces on the structure; (ii) the hydrodynamic loads are transferred to the structural dynamic model to derive the motion quantities of the system; (iii) the new mesh configuration is evaluated based on the motion quantities of the system and the interpolation stencils are updated; (iv) the N–S equations are then solved on the new mesh configuration. This FSI loop is repeated every time step until the end of the simulation. The same numerical methods as well as the fluid–structure interaction procedures have been employed in our previous studies on the FIV of a circular cylinder and a circular cylinder with a base column [38,39].

3. Problem description

This section starts with an introduction to the simulation parameters, followed by the descriptions of the computational domain and the boundary conditions. In addition, the validation of the present numerical method together with the mesh dependency tests is given.

3.1. Simulation parameters

2D numerical simulation is performed for the FIV of an elastically supported circular cylinder fitted with a rigid splitter plate (i.e., the rotational and flexural motion of the splitter plate is constrained). The diameter of the circular cylinder is D and the length of the splitter plate is L. The dimensionless splitter plate length is subsequently expressed as $L^* = L/D$. The splitter plate has a thickness of $t_p = 0.06D$. The mass ratio is kept constant at 10. Zero damping is considered for the cylinder-plate assembly in order to maximise its FIV response. The system is allowed to vibrate in the CF direction only. Re is fixed at 100 in the present simulation. It was discussed by Serson et al. [9] that the splitter plate had a stabilising effect on the flow which delayed the appearance of three-dimensional (3D) structures to higher Re. In their study, 2D flow persisted up to $Re = 200$. The flow at $Re = 100$ in this study is essentially 2D and laminar and it can be modelled by directly solving the 2D unsteady incompressible N–S equations without the potential uncertainties introduced by the utilisation of turbulence models. Similar 2D and laminar assumptions were also adopted by Law and Jaiman [31], Sun et al. [28], Zhu et al. [27] and Tang et al. [29] in their simulations of FIV of a cylinder-plate assembly at similar Re values. Previous studies by Leontini et al. [40],Bao et al. [41] and Wang et al. [38] unveiled that the FIV of rigid structures at low Re shared comparable response features to that at high Re. Moreover, studies on the FIV of the cylinder-plate assembly at low Re are also of fundamental research interest from a flow physics point of view. V_r in this study is gradually varied from 2 to 26 with an increment of 1. Seven different L^* values are considered, i.e., $L^* = 0$ (corresponding to the plain cylinder), 0.25, 0.5, 0.75, 1, 1.5 and 2. The choice of the L^* range stems from the following considerations: $L^* = 0$ serves as the baseline case where there is no splitter plate. According to the experimental data of Stappenbelt [22] and Sun et al. [24], the FIV was significantly reduced once L^* was beyond 2. As this paper is mainly focused on the FIV characteristics, cases with longer plate where the FIV is suppressed are beyond the scope of the present research and the maximum L^* value is consequently selected as 2.

3.2. Computational domain and boundary conditions

A $75D \times 50D$ rectangular computational domain as shown in Fig. 2(a) is utilised in the present study. The centre of gravity (COG) of the oscillating system coincides with the origin of the Cartesian coordinate system which is located $25D$ downstream the inlet boundary and $25D$ away from the two lateral boundaries. Fig. 2(b) depicts the overall computational mesh and a close-up of the mesh around the cylinder-plate assembly. The following are the details about the boundary conditions in the simulation: The surface of the cylinder-plate assembly is assumed to be smooth where a no-slip boundary condition with $\mathbf{u} = (0, \dot{y})$ is used. The freestream velocity is applied to the inlet boundary as $\mathbf{u} = (U_\infty, 0)$, while the gradients of the fluid velocity in the streamwise direction are set to zero on the outlet boundary. For the two transverse boundaries, a free-slip boundary condition with the velocity

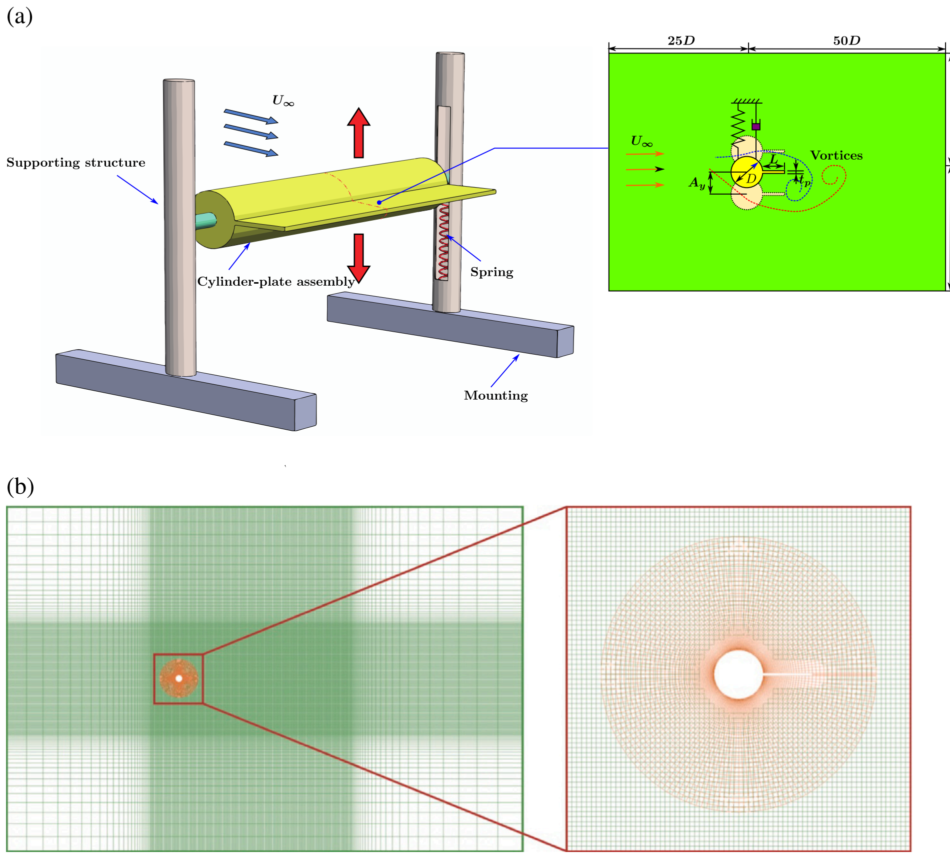

Fig. 2. (a) Schematics of the FIV of a circular cylinder with a rigid splitter plate and the computational domain and (b) computational mesh and a close-up of the mesh around the cylinder-plate assembly.

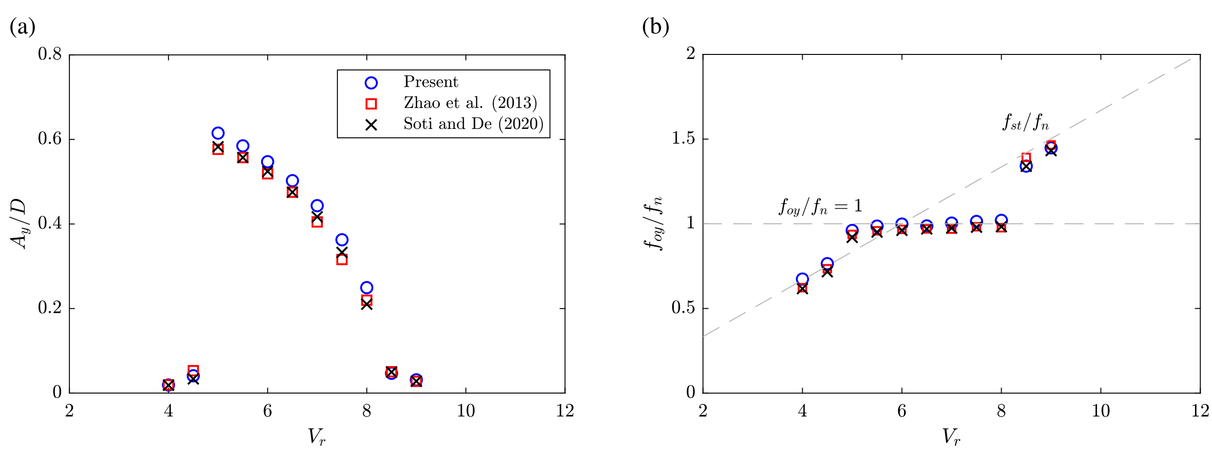

Fig. 3. Comparisons of the amplitude and frequency (A_y/D and f_{oy}/f_n) responses for the VIV of a plain cylinder between the present results and those by Zhao et al. [42] and Soti and De [43]: (a) amplitude response and (b) frequency response. Blue circles—present results, red squares—Zhao et al. [42] and black crosses–Soti and De [43]; in (b): horizontal grey dashed line denotes nondimensional oscillation frequency $f_{oy}/f_n = 1$ and inclined grey dashed line represents dimensionless Strouhal frequency f_{st}/f_n.

in the normal direction of the boundaries being zero is employed. In terms of the boundary conditions for the pressure, a zero gradient boundary condition is adopted for the pressure on all the boundaries except the outlet one on which a zero reference pressure ($p_{ref} = 0$) is imposed. For the motion quantities of the system, zero displacement and velocity ($y = 0$ and $\dot{y} = 0$) are assigned as the initial conditions. Adaptive time-step sizes are employed in the present simulation and the time-step size is adjusted to meet the Courant–Friedrichs–Lewy (CFL) condition that the maximum Courant number ($C_{o\max}$) is less than 0.5.

3.3. Validation and verification

Simulation is conducted for the VIV of an elastically mounted circular cylinder to validate the present numerical method. In order to facilitate the comparison, the same flow and structural parameters as those in Zhao et al. [42] and Soti and De [43] are used with $Re = 100$, $m^* = 10$ and $\zeta = 0$. The V_r range is from 4 to 9. Fig. 3 shows the comparisons of the amplitude and frequency responses for the transverse vibration of the bare cylinder as functions of V_r.

Table 1
Comparison of the simulation results from three different meshes.

Mesh	N_c	N_b	A_y/D	f_{oy}/f_n	$\overline{C}_x$	C'_x	C'_y
M1	6316	50622	1.0040	0.7711	1.2423	0.1053	1.1606
M2	8851	71400	0.9953	0.7615	1.2411	0.1048	1.1640
M3	12403	102720	0.9889	0.7542	1.2404	0.1045	1.1643

Following the benchmark cases [42,43], the vibration amplitude in the CF direction A_y is defined as $A_y = (y_{\max} - y_{\min})/2$, where $y_{\max}$ and $y_{\min}$ are respectively the maximum and minimum displacements. The Lomb–Scargle Periodogram [44] is used to determine the oscillation frequency f_{oy} from unevenly sampled displacement data. It can be seen from the figure that the variations of the nondimensional vibration amplitude A_y/D and normalised oscillation frequency f_{oy}/f_n agree well with those in the existing publications. The maximum $A_y/D \approx 0.6$ appears at the same V_r of 5 as the two previous studies and the computed lock-in ranges in the present and the other simulations are also identical with V_r = 5–8. The overall agreement indicates that the present numerical method is reliable for predicting the FIV response of an elastically mounted structure with reasonable accuracy at low Re.

Before systematically investigating the FIV characteristics of a circular cylinder attached with different splitter plates, a mesh dependency study is performed to make sure that further refinement of the mesh has negligible influence on the numerical results. The parameters of the chosen cylinder-plate assembly for the mesh dependency tests are $m^* = 10$, $\zeta = 0$ and $L^* = 1$ with V_r being 13 at $Re = 100$. Three different meshes are generated with a grid refinement factor approximately $r = \sqrt{2}$ as suggested by Terziev et al. [45] and Song et al. [46]. The effect of the mesh density on the simulation results is examined. The comparison of the simulation results from three different mesh systems is tabulated in Table 1. N_c and N_b are the numbers of elements for the component and background meshes, respectively. The in-line (IL) and CF force coefficients are given by $C_x = F_x/\left(0.5\rho U_\infty^2 D\right)$ and $C_y = F_y/\left(0.5\rho U_\infty^2 D\right)$, where $F_x = \int_\Gamma \left(\boldsymbol{\sigma}_f \cdot \mathbf{n}\right) \cdot \mathbf{n}_x d\Gamma$ and $F_y = \int_\Gamma \left(\boldsymbol{\sigma}_f \cdot \mathbf{n}\right) \cdot \mathbf{n}_y d\Gamma$ are respectively the IL and CF hydrodynamic forces. Herein, Γ denotes the surface of the cylinder-plate system, the fluid stress tensor $\boldsymbol{\sigma}_f$ is considered as a sum of a pressure contributed stress component and a viscous contributed stress component: $\boldsymbol{\sigma}_f = -p\mathbf{I} + \mu\left(\nabla\mathbf{u} + (\nabla\mathbf{u})^T\right)$, where $\mathbf{I}$ represents the unit tensor, μ stands for the dynamic viscosity of the fluid, $\mathbf{n}$ is the outward-pointing vector normal to the surface of the cylinder-plate assembly and $\mathbf{n}_x$ and $\mathbf{n}_y$ are the Cartesian components of $\mathbf{n}$. $\overline{C}_x$ represents the mean IL force coefficient, C'_x denotes the root mean square (RMS) value of the fluctuating IL force coefficient and C'_y is the RMS value of the oscillating CF force coefficient. As shown in the table, the maximum difference between M1 (coarse mesh) and M2 (medium mesh) is around 1.2568% and is observed for f_{oy}/f_n. The maximum difference between M2 and M3 (fine mesh) also appears in f_{oy}/f_n, whereas it reduces to 0.9646%. Balancing the accuracy and the computational cost, the mesh density of M2 is selected and the computational meshes for L^* other than 1 are generated based on this mesh density.

Our previous study showed that the numerical uncertainty of the model was governed by the grid uncertainty and other sources of errors such as the time-step size and iterative convergence were almost negligible [47]. In this study, the grid convergence index (GCI) is utilised to quantify the numerical uncertainty. The GCI requires three grid solutions. Here, the data from the three grids of the mesh dependency test in Table 1 are employed. Systematic refinement of the grid twice with $r = \sqrt{2}$ yields the coarse (f_3), medium (f_2) and fine (f_1) solutions. According to Stern et al. [48], the order of accuracy P can be estimated by using the following equations:

$$P = \frac{\ln\left(\varepsilon_{32}/\varepsilon_{21}\right)}{\ln(r)} \tag{6}$$

$$\varepsilon_{i+1,i} = f_{i+1} - f_i \tag{7}$$

Table 2
Numerical uncertainty assessment results.

	ε_{32}	ε_{21}	p	GCI_{32}	GCI_{21}
A_y/D	0.0087	0.0064	0.8985	2.9890%	2.2033%
f_{oy}/f_n	0.0096	0.0073	0.7912	4.9798%	3.8221%
$\overline{C}_x$	0.0011	0.0007	1.2451	0.2125%	0.1381%
C'_x	0.0005	0.0003	1.4382	0.8688%	0.5292%
C'_y	−0.0034	−0.0003	7.5111	0.0296%	0.0022%

where ε_{21} is the difference between the medium and fine solutions and ε_{32} is the difference between the coarse and medium solutions. p is used to predict the GCI uncertainty:

$$GCI_{i+1,i} = F_s \frac{\left|\varepsilon_{i+1,i}\right|}{f_i\left(r^P - 1\right)} \tag{8}$$

The safety factor F_s is selected as 1.25 [49]. The results for the uncertainty assessment are summarised in Table 2. It can be seen from the table that there is a reduction in the GCI value for successive grid refinements ($GCI_{21} < GCI_{32}$) about each of the five variables. The GCI uncertainty is less than 5% even for the coarse grid. Such performance is deemed acceptable.

4. Results and discussion

In this section, the influence of the splitter plate length on the amplitude and frequency responses, the phase differences between the transverse force coefficients and the cross-flow displacement, the hydrodynamic coefficients as well as the wake flow patterns is analysed.

4.1. Amplitude and frequency responses

The variations of A_y/D and f_{oy}/f_n of the cylinder-plate assembly with V_r for different L^* are demonstrated in Fig. 4. As shown in Fig. 4(a), the A_y/D curves of small L^* values (L^* = 0.25 and 0.5) resemble that of the plain cylinder ($L^* = 0$) and demonstrate classic VIV response characteristics. With the increase in L^*, the onset of VIV is delayed slightly from V_r = 5 to V_r = 6, which can be attributed to the decrease in St from 0.167 for the plain cylinder to 0.149 for $L^* = 0.5$. The decrease in St for the small L^* cases was also reported by Apelt et al. [2] and Anderson and Szewczyk [5]. As L^* is increased from 0 to 0.5, there is a significant increase in the maximum attainable A_y/D from a value of 0.6 typical for the 1DOF VIV at low Re to around 1 comparable with the 1DOF VIV at subcritical Re. Another stunning feature is the widening of the V_r range corresponding to large A_y/D with increasing L^*. Larger-amplitude oscillations are witnessed only in the range of V_r = 5–8 at $L^* = 0$ while this range is enlarged to V_r = 6–18 in the case of $L^* = 0.5$. Moreover, the slope of the initial branch (IB) decreases with the increase in L^* indicating the enhancement of the stabilisation effect of the rigid splitter plate [24]. In terms of the frequency responses in Fig. 4(b), the f_{oy}/f_n curves of L^* = 0, 0.25 and 0.5 nearly coincide with each other at low V_r. Similar to the amplitude responses, the onset of the frequency lock in is also postponed a little as L^* is increased. The plateau of f_{oy}/f_n is apparently prolonged with a slight decrease in its value from unity to around 0.93 when L^* is varied from 0 to 0.5. After the frequency synchronisation, f_{oy}/f_n maintains a linearly increasing trend along the Strouhal frequency for each configuration. As mentioned earlier, St for the system with a longer splitter plate is slightly lower leading to the discrepancies in the f_{oy}/f_n curves at high V_r.

In the present study, galloping-type responses characterised by the low frequency oscillations whose amplitude would build up monotonically with the flow velocity emerge when $L^* \geq 0.75$. As discussed by Sun et al. [24], the FIV in the L^* = 0.75 case can be categorised as the combined VIV-galloping pattern. For this specific L^*, A_y/D increases steadily with the increase in V_r. Then, a local peak of A_y/D is

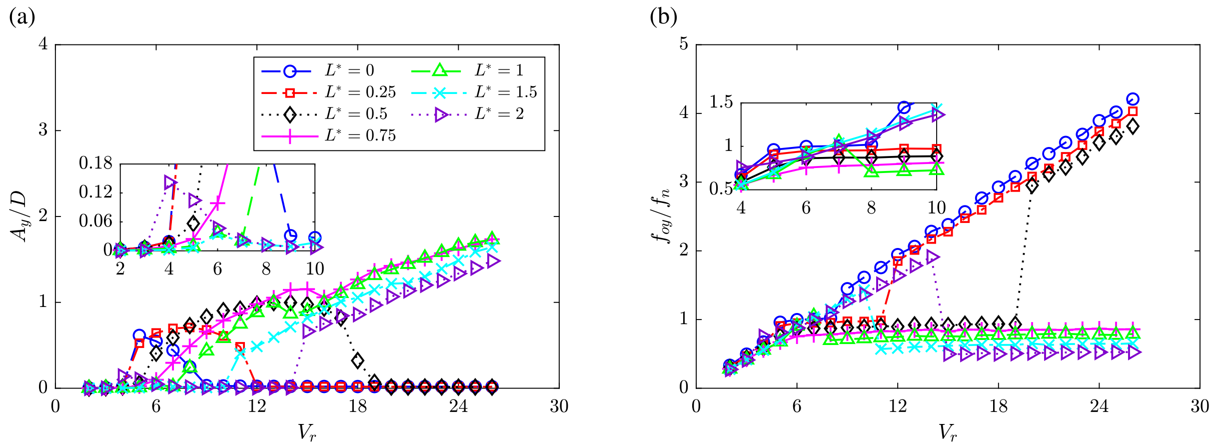

Fig. 4. Variations of the amplitude and frequency (A_y/D and f_{oy}/f_n) responses of the cylinder-plate assembly with the reduced velocity (V_r) for different nondimensional splitter plate length (L^*) values: (a) amplitude response and (b) frequency response. Blue circles–$L^* = 0$, red squares–$L^* = 0.25$, black diamonds–$L^* = 0.5$, pink plus signs–$L^* = 0.75$, green upward-pointing triangles–$L^* = 1$, cyan crosses–$L^* = 1.5$ and purple right-pointing triangles–$L^* = 2$.

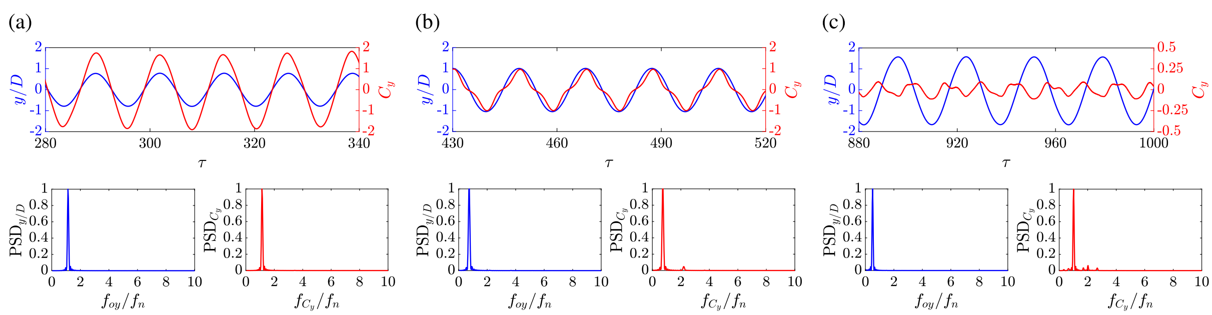

Fig. 5. Time histories and normalised power spectral density (PSD) plots of the displacement and force coefficient in the transverse direction (y/D and C_y) for the nondimensional splitter plate length $L^* = 0.75$ and different reduced velocities (V_r): (a) $V_r = 10$, (b) $V_r = 16$ and (c) $V_r = 24$. In each subfigure, the upper plot includes the time histories of y/D and C_y, the lower left plot presents the normalised PSD plot of y/D and the normalised PSD plot of C_y is depicted in the lower right plot; blue lines–y/D and red lines–C_y.

observed at $V_r = 15$. After the peak, A_y/D starts to rise up with a slope different from the one in the range of $V_r = 6$–14. A similar kink in the galloping response was also observed by Bearman et al. [50], Nemes et al. [51], Bourguet and Jacono [52], Sahu et al. [53], Zhao et al. [54] and Sun et al. [28]. As for the f_{oy}/f_n curve, it first follows the St frequency of the stationary cylinder-plate system. Then, it flattens out at V_r around 6 with a frequency lower than the synchronised frequencies of $L^* = 0$–0.5. Beyond $V_r = 6$, no significant deviation in the variation trend of the f_{oy}/f_n is found. Here, the time histories and normalised power spectral density (PSD) plots of y/D and C_y for $V_r = 10$ (before the kink), 16 (near the kink) and 24 (after the kink) are presented in Fig. 5. The time series are drawn with respect to the nondimensional time $\tau = tU_\infty/D$ and each PSD plot is normalised with its maximum power. It can be seen that with the increase in V_r, a third harmonic frequency component appears in C_y, which agrees with the conclusion of Bearman et al. [50] that the kink in the response could be attributed to the transverse force component at three times the oscillation frequency. Considering the contributions of both the lift and drag forces in the total transverse force, the third harmonic component could be easily found for the cylinder fitted with a rigid splitter plate. One may refer to Sun et al. [24] for the detailed analyses.

The amplitude and frequency response curves of $L^* = 1$, 1.5 and 2 accord with the WVIV-galloping pattern. A narrow region of weak VIV with $A_y/D < 0.15$ is found at low V_r. The local peaks of $L^* = 1$ and 1.5 are observed at an identical V_r of 6 with values around 0.035. As L^* is increased to 2, the local peak of A_y/D shifts to a lower V_r of 4 and its value increases to 0.14. A_y/D falls after reaching its local peak. The system with $L^* = 1$ enters the galloping response first at $V_r = 7$. The onset of galloping is delayed to higher V_r with increasing L^*. An obvious kink is observed for $L^* = 1$ at V_r around 13 and 14 before the A_y/D curve switches to another increasing rate. As L^* is increased, the kink gradually diminishes and the slope of the galloping branch becomes milder. Fig. 6 shows the time histories and normalised PSD plots of y/D and C_y at $V_r = 4$ (WVIV peak), 10 (onset of galloping) and 24 (high end of the V_r range) for $L^* = 2$. It is demonstrated that the third harmonic frequency component with increasing V_r is not as obvious as that in Fig. 5. Therefore, no evident kink appears in the response curve. The frequency responses in Fig. 4(b) show that the f_{oy}/f_n values of $L^* = 1$, 1.5 and 2 increase along their own St frequencies without evident synchronisation with their natural frequencies. Once galloping is initiated, f_{oy}/f_n drops and keeps nearly constant throughout the galloping branch. The larger L^* is associated with a lower f_{oy}/f_n in the galloping regime. Similar conclusion that f_{oy}/f_n decreased with increasing L^* was also reached in the numerical study of Sun et al. [28]. Analogous to the $L^* = 0.75$ case, there are no significant variations in the frequency responses around the kinks.

As argued by Govardhan and Williamson [55], the branching behaviours of the VIV of an elastically supported circular cylinder are associated with the jumps in the vortex and total phases (ϕ_{vortex} and ϕ_{total}). ϕ_{vortex} is the phase difference between vortex force F_{vortex} and y while ϕ_{total} is the phase difference between F_y and y. F_{vortex} is related in a definite way to the vortex dynamics and to the convection of vorticity which can be computed by $F_{vortex} = F_y - F_{potential}$ with the potential added mass force $F_{potential} = -C_a m_d \ddot{y}$, where C_a is the potential

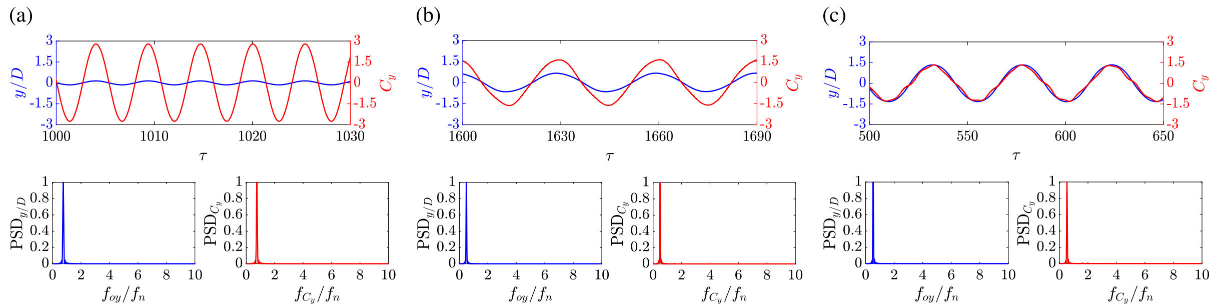

Fig. 6. Time histories and normalised power spectral density (PSD) plots of the displacement and force coefficient in the transverse direction (y/D and C_y) for the nondimensional splitter plate length $L^* = 2$ and different reduced velocities (V_r): (a) $V_r = 4$, (b) $V_r = 15$ and (c) $V_r = 24$. In each subfigure, the upper plot includes the time histories of y/D and C_y, the lower left plot presents the normalised PSD plot of y/D and the normalised PSD plot of C_y is depicted in the lower right plot; blue lines—y/D and red lines—C_y.

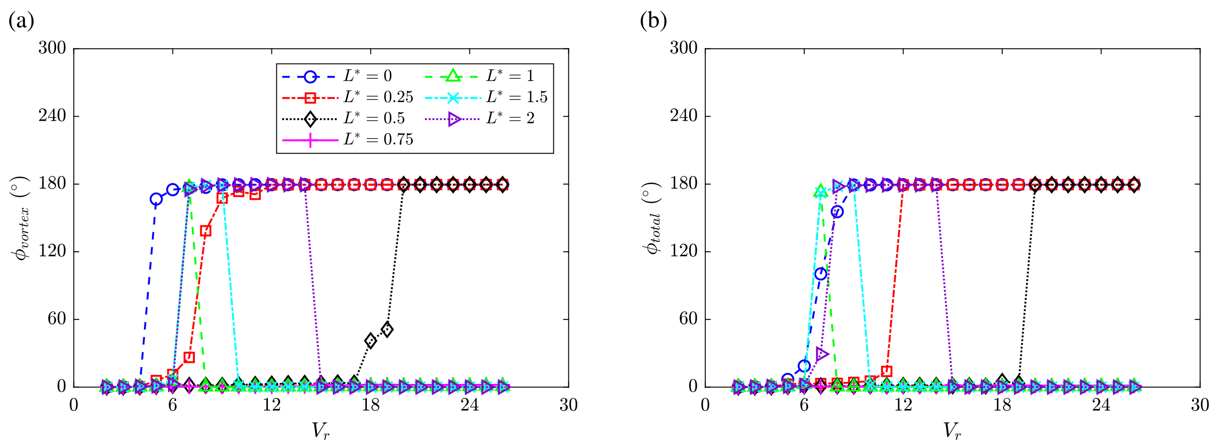

Fig. 7. Vortex and total phases (ϕ_{vortex} and ϕ_{total}) of the cylinder-plate assembly as functions of the reduced velocity (V_r) for different nondimensional splitter plate length (L^*) values: (a) ϕ_{vortex} and (b) ϕ_{total}. Blue circles—$L^* = 0$, red squares—$L^* = 0.25$, black diamonds—$L^* = 0.5$, pink plus signs—$L^* = 0.75$, green upward-pointing triangles—$L^* = 1$, cyan crosses—$L^* = 1.5$ and purple right-pointing triangles—$L^* = 2$.

added mass coefficient of the oscillating system. It was shown in the previous studies [38,39] that the transition between the IB and upper branch (UB) involved a jump in ϕ_{vortex} and the transition between the UB and lower branch (LB) was associated with a jump in ϕ_{total}. Fig. 7 presents ϕ_{vortex} and ϕ_{total} of the cylinder-plate assembly as functions of V_r for different L^* values. For the plain cylinder, the VIV response transits to the UB at $V_r = 5$ with ϕ_{vortex} leaping to 180° and it enters the LB when $V_r = 8$ and ϕ_{total} increases to around 180°. In the desynchronisation range, both phases remain at 180°. In the case of $L^* = 0.25$, the transition between the IB and UB takes place in the range of $V_r = 5$–9 and that between UB and LB occurs at $V_r = 11$ and 12. For $L^* = 0.5$, the IB persists up to $V_r = 16$ and between $V_r = 19$ and 20, the response switches to the LB. The combined VIV-galloping oscillation pattern at $L^* = 0.75$ features ϕ_{vortex} and ϕ_{total} being 0° within the V_r range considered in the present study. This indicates that the vibration response transits from the IB directly to galloping. When L^* is increased to 1, ϕ_{vortex} and ϕ_{total} experience 180° jumps at the onset of the galloping branch, i.e., $V_r = 7$ and they both immediately fall back to 0°, then F_{vortex} and F_y stay in phase with y. The variations of ϕ_{vortex} and ϕ_{total} with V_r are quite similar for $L^* = 1.5$ and 2. Both ϕ_{vortex} and ϕ_{total} increase from 0° to 180° in the LB, whereas there exists a slight increase in the V_r where ϕ_{total} experiences the 0° to 180° jump. The same trends as the $L^* = 1$ case are observed for $L^* = 1.5$ and 2 that the transition from the WVIV to galloping is associated with the 180° to 0° drop in both ϕ_{vortex} and ϕ_{total}. When the system is subject to galloping, ϕ_{vortex} and ϕ_{total} maintain at 0° reflecting that F_{vortex} and F_y are in phase with y.

4.2. Hydrodynamic coefficients

Fig. 8 shows the variations of $\overline{C}_x$, C'_x and C'_y with V_r for different L^* values. It can be seen from Fig. 8(a) and (b) that the shapes of the $\overline{C}_x$ and C'_x curves for each L^* are quite alike. In the VIV cases ($L^* = 0$, 0.25 and 0.5), $\overline{C}_x$ and C'_x at the onset of the IB and in the desynchronisation range are around their counterparts of the stationary system. The peaks of $\overline{C}_x$ and C'_x appear near the low ends of their lock-in ranges with $L^* = 0$ and 0.25 at V_r around 5 and $L^* = 0.5$ at V_r around 8. With the increase in L^*, the peaks of $\overline{C}_x$ and C'_x decrease. For combined VIV-galloping at $L^* = 0.75$, $\overline{C}_x$ and C'_x first increase with V_r and near the kink, they decrease slightly and then level off. When the oscillations are in the WVIV-galloping pattern, the first peaks of $\overline{C}_x$ and C'_x are associated with the peaks in the WVIV regime. Then, they both fall and at the kinks, they start to increase and reach the plateaus. The value of the $\overline{C}_x$ plateau is lower for larger L^*, whereas the C'_x values at high V_r for $L^* = 0.75$, 1, 1.5 and 2 almost collapse into a single curve. Compared to the IL force coefficient curves, the C'_y curves for different L^* values are more scattered. The C'_y values at the onset of the VIV for $L^* = 0$, 0.25 and 0.5 are around 0.2–0.3 and the peaks are found at V_r about 5 and 6. The peak of C'_y for the cylinder-plate assembly is significantly higher than that of the plain cylinder. C'_y of the bare cylinder falls to around 0 at $V_r = 7$ and then increases to 0.2 in the desynchronisation branch. C'_y values of $L^* = 0.25$ and 0.5 gradually decrease to similar levels beyond their peak values and there is a slight decrease in the desynchronised C'_y as L^* is increased. The C'_y curve of $L^* = 0.75$ rises at low V_r and peaks at $V_r = 9$. After that,

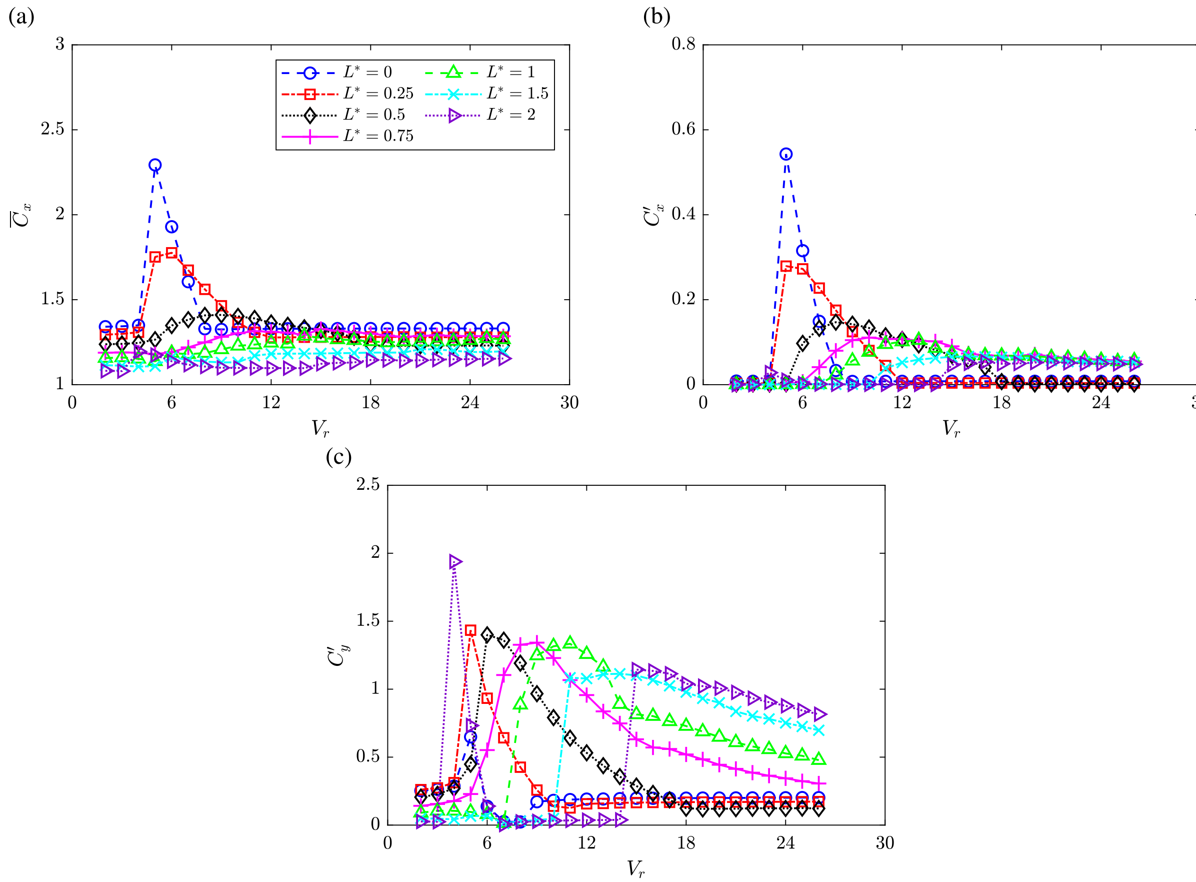

Fig. 8. Variations of the mean and root mean square (RMS) values of the in-line force coefficient ($\overline{C}_x$ and C'_x) and the RMS value of cross-flow force coefficient (C'_y) with the reduced velocity (V_r) for different nondimensional splitter plate length (L^*) values: (a) $\overline{C}_x$, (b) C'_x and (c) C'_y. Blue circles—$L^* = 0$, red squares—$L^* = 0.25$, black diamonds—$L^* = 0.5$, pink plus signs–$L^* = 0.75$, green upward-pointing triangles—$L^* = 1$, cyan crosses—$L^* = 1.5$ and purple right-pointing triangles—$L^* = 2$.

it keeps on decreasing until the highest V_r considered. In terms of the WVIV-galloping cases ($L^* = 1$, 1.5 and 2), a local peak of C'_y is found to be associated with the first peak of A_y/D and it subsequently drops to 0. As V_r is further increased, the second peak of C'_y is reached at the beginning of the galloping branch. When the system is subject to galloping, C'_y decreases with increasing V_r. In addition, the C'_y in the galloping regime is larger for longer splitter plate length.

F_y of the cylinder-plate assembly can be expressed in terms of the force coefficient in phase with $\dot{y}$ (the excitation coefficient C_{ey}) and the force coefficient in phase with $\ddot{y}$ (the added mass coefficient C_{ay}) as

$$F_y(t) = \frac{\rho U_\infty^2 D}{2\sqrt{2}\dot{y}_{rms}} C_{ey}\dot{y}(t) - \frac{\rho\pi D^2}{4} C_{ay}\ddot{y}(t) \tag{9}$$

where $\dot{y}_{rms}$ is the RMS value of the CF velocity $\dot{y}(t)$.

The predicted vortex-induced force in the transverse direction F_p can be given by

$$F_p(t) = \frac{\rho U_\infty^2 D}{2\sqrt{2}\dot{y}_{rms}} C_{ey}\dot{y}(t) - \frac{\rho\pi D^2}{4} C_{ay}\ddot{y}(t) \tag{10}$$

The least squares method as used by Song et al. [56] and Xu et al. [57] is adopted to derive the two hydrodynamic coefficients by minimising the sum of the squared error between F_p and F_y for a certain interval of time, which can be expressed as

$$\begin{aligned} e^2 &= \sum_{i=1}^{N_s} \left[F_p(t_i) - F_y(t_i)\right]^2 \\ &= \sum_{i=1}^{N_s} \left[\frac{\rho D U_\infty^2}{2\sqrt{2}\dot{y}_{rms}} C_{ey}\dot{y}(t_i) - \frac{\rho\pi D^2}{4} C_{ay}\ddot{y}(t_i) - F_y(t_i)\right]^2 = \min \end{aligned} \tag{11}$$

where N_s is the total number of samples. Rearranging the right-hand side of Eq. (8) gives

$$\begin{aligned} e^2 = {} & \left(\frac{\rho U_\infty^2 D}{2\sqrt{2}\dot{y}_{rms}}\right)^2 C_{ey}^2 \sum_{i=1}^{N_s} \left[\dot{y}(t_i)\right]^2 - \frac{\rho^2 \pi U_\infty^2 D^3}{4\sqrt{2}\dot{y}_{rms}} C_{ey} C_{ay} \sum_{i=1}^{N_s} \left[\dot{y}(t_i)\,\ddot{y}(t_i)\right] \\ & - \frac{\rho U_\infty^2 D}{\sqrt{2}\dot{y}_{rms}} C_{ey} \sum_{i=1}^{N_s} \left[F_y(t_i)\,\dot{y}(t_i)\right] \\ & + \frac{\left(\rho\pi D^2\right)^2}{16} C_{ay}^2 \sum_{i=1}^{N_s} \left[\ddot{y}(t_i)\right]^2 + \frac{\rho\pi D^2}{2} C_{ay} \sum_{i=1}^{N_s} \left[F_y(t_i)\,\ddot{y}(t_i)\right] \\ & + \sum_{i=1}^{N_s} \left[F_y(t_i)\right]^2 \end{aligned} \tag{12}$$

It is assumed that $G_1 = \sum_{i=1}^{N_s}\left[\dot{y}(t_i)\right]^2$, $G_2 = \sum_{i=1}^{N_s}\left[\dot{y}(t_i)\,\ddot{y}(t_i)\right]$, $G_3 = \sum_{i=1}^{N_s}\left[F_y(t_i)\,\dot{y}(t_i)\right]$, $G_4 = \sum_{i=1}^{N_s}\left[\ddot{y}(t_i)\right]^2$ $G_5 = \sum_{i=1}^{N_s}\left[F_y(t_i)\,\ddot{y}(t_i)\right]$ and $G_6 = \sum_{i=1}^{N_s}\left[F_y(t_i)\right]$.

Eq. (9) can be simplified as

$$\begin{aligned} e^2 = {} & \left(\frac{\rho U_\infty^2 D}{2\sqrt{2}\dot{y}_{rms}}\right)^2 C_{ey}^2 G_1 - \frac{\rho^2\pi U_\infty^2 D^3}{4\sqrt{2}\dot{y}_{rms}} C_{ey} C_{ay} G_2 - \frac{\rho U_\infty^2 D}{\sqrt{2}\dot{y}_{rms}} C_{ey} G_3 \\ & + \frac{\left(\rho\pi D^2\right)^2}{16} C_{ay}^2 G_4 + \frac{\rho\pi D^2}{2} C_{ay} G_5 + G_6 \end{aligned} \tag{13}$$

Minimising e^2 with respect to C_{ay} and C_{ey} by

$$\frac{\partial e^2}{\partial C_{ay}} = 0 \quad \frac{\partial e^2}{\partial C_{ey}} = 0 \tag{14}$$

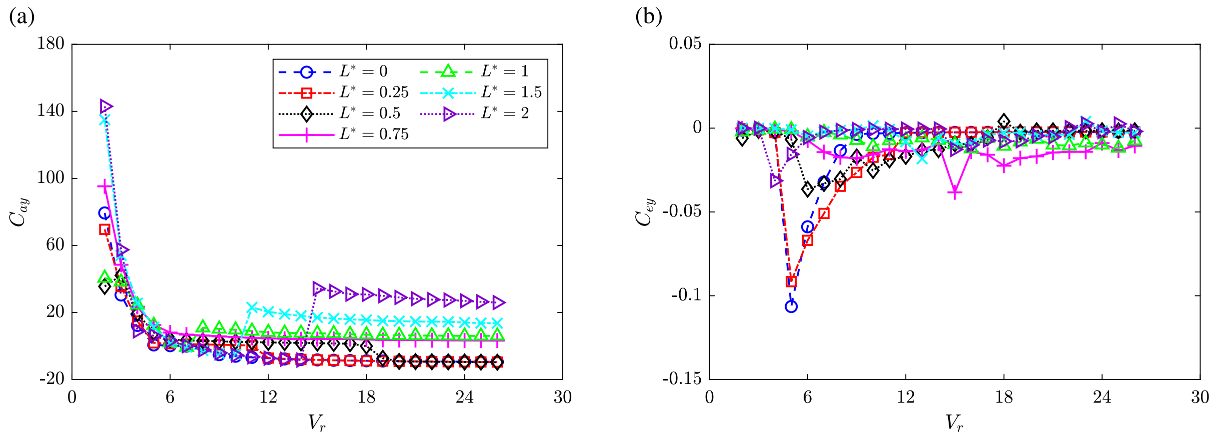

Fig. 9. Added mass and excitation coefficients in the cross-flow direction (C_{ay} and C_{ey}) as functions of the reduced velocity (V_r) for different nondimensional splitter plate length (L^*) values: (a) C_{ay} and (b) C_{ey}. Blue circles—$L^* = 0$, red squares—$L^* = 0.25$, black diamonds—$L^* = 0.5$, pink plus signs—$L^* = 0.75$, green upward-pointing triangles—$L^* = 1$, cyan crosses—$L^* = 1.5$ and purple right-pointing triangles—$L^* = 2$.

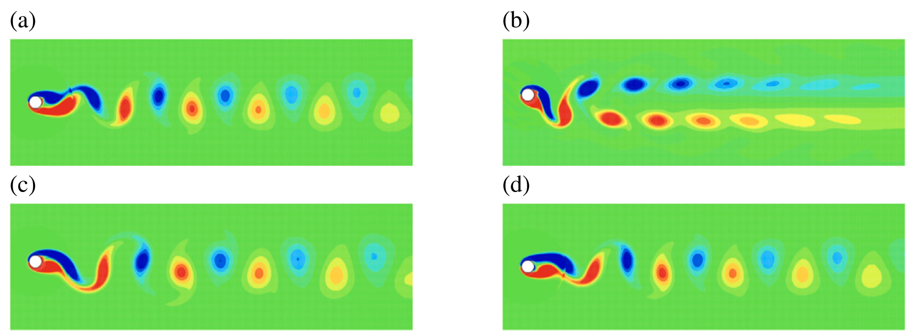

Fig. 10. Vortex shedding modes of the nondimensional splitter plate length $L^* = 0$ case at different reduced velocities (V_r): (a) $V_r = 4$, (b) $V_r = 5$, (c) $V_r = 7$ and (d) $V_r = 10$. The contours are the nondimensional spanwise vorticity component ω_z.

Substituting Eq. (10) into Eq. (11) gives

$$\begin{aligned} &\frac{1}{2}\left(\frac{\rho U_\infty^2 D}{\sqrt{2}\dot{y}_{rms}}\right)^2 C_{ey}G_1 - \frac{\rho^2\pi U_\infty^2 D^3}{4\sqrt{2}\dot{y}_{rms}}C_{ay}G_2 - \frac{\rho U_\infty^2 D}{\sqrt{2}\dot{y}_{rms}}G_3 = 0 \\ &-\frac{\rho^2\pi U_\infty^2 D^3}{4\sqrt{2}\dot{y}_{rms}}C_{ey}G_2 + \frac{\left(\rho\pi D^2\right)^2}{8}C_{ay}G_4 + \frac{\rho\pi D^2}{2}G_5 = 0 \end{aligned} \tag{15}$$

Solving Eq. (12), C_{ay} and C_{ey} can be calculated by

$$C_{ey} = \frac{2\sqrt{2}\dot{y}_{rms}}{\rho U^2 D}\frac{G_2G_5 - G_3G_4}{G_2^2 - G_1G_4},\quad C_{ay} = \frac{4}{\rho\pi D^2}\frac{G_1G_5 - G_2G_3}{G_2^2 - G_1G_4} \tag{16}$$

When a body is subject to FIV, C_{ay} and C_{ey} can vary significantly [58,59]. C_{ay} plays a complex role in determining the natural and oscillation frequencies of the system [60] while C_{ey} defines the energy transfer between the fluid and the structure [61]. C_{ay} and C_{ey} as functions of V_r for different L^* values are depicted in Fig. 9. As shown in Fig. 9(a), the variation trends of the C_{ay} curves in the VIV cases ($L^* = 0$, 0.25 and 0.5) generally agree with that in Wang et al. [38]. C_{ay} decreases with the increase in V_r before the lock-in range. When the frequency synchronisation occurs, C_{ay} reaches a plateau. The cylinder-plate assembly with a larger L^* has a slightly higher plateau value and this is also reflected by its lower f_{oy}/f_n in Fig. 4(b). There is a further decrease in C_{ay} as the response enters the desychronisation branch and the three curves almost coincide with each other having a negative value when $f_{oy}/f_n > 1$, which was also observed by Srinil et al. [62]. The declination of C_{ay} for $L^* = 0.75$ is relatively steep when $V_r = 2$–6. Beyond $V_r = 6$, C_{ay} only varies in a small range of 3–7 although the overall trend is still decreasing. As for $L^* = 1$, 1.5 and 2, their C_{ay} values drop significantly in the WVIV region. The C_{ay} curves experience abrupt leaps when galloping is initiated. In the galloping range, C_{ay} decreases at much slower rates than those in the WVIV regime. Another important feature of the galloping response is that its C_{ay} is always greater than 0. As a consequence, the corresponding f_{oy}/f_n is lower than 1. Fig. 9(b) demonstrates that C_{ey} in the zero damping system is mostly negative indicating that the energy is dissipated through the hydrodynamic damping. When the system is undergoing VIV, the troughs of C_{ey} in the cases of $L^* = 0$ and 0.25 appear at identical V_r of 5. That of $L^* = 0.5$ is postponed to $V_r = 6$ with its magnitude increasing slightly. At the onset of VIV and in the desynchronisation range, C_{ey} approaches 0. Negative C_{ey} values are also observed for the combined VIV-galloping case and the WVIV-galloping cases with zero damping. The troughs in their C_{ey} curves are associated with the kinks in the response curves and the magnitudes of the troughs are larger than those of $L^* = 0$ and 0.25.

4.3. Wake patterns

In order to reveal the underlying mechanisms of certain FIV behaviours, the wake patterns behind the cylinder-plate assembly at different V_r values are analysed by plotting the nondimensional spanwise vorticity contours which is defined as $\omega_z = (\partial v/\partial x - \partial u/\partial y)/\left(U_\infty/D\right)$. It can be seen from Fig. 10 that the plain cylinder possesses typical low *Re* VIV wake patterns analogous to those in Bao et al. [41] and Wang et al. [38]. The vortex shedding of the $L^* = 0$ case demonstrates a 2S mode (two single vortices are shed per vibration cycle). At the onset of the IB, a single-row vortex street similar to the Kármán vortex street is observed. With the increase in A_y/D, the wake changes to a double-row configuration. As the response enters the LB around $V_r = 7$, the vortex street returns to a single row. In the desynchronisation branch, the wake width further reduces. When L^* is increased to 0.25, a 2S

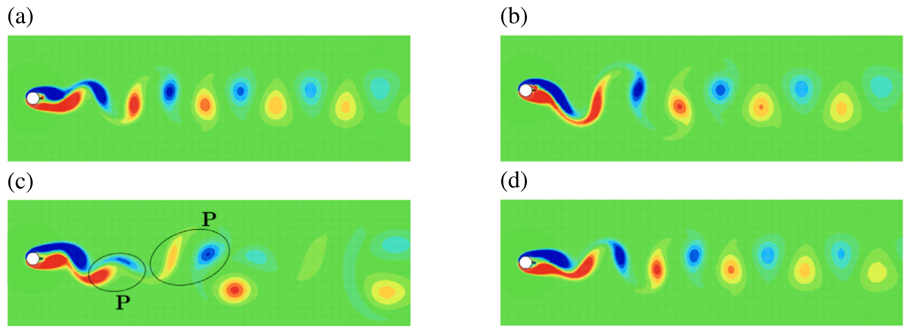

Fig. 11. Vortex shedding modes of the nondimensional splitter plate length $L^* = 0.25$ case at different reduced velocities (V_r): (a) $V_r = 4$, (b) $V_r = 7$, (c) $V_r = 11$ and (d) $V_r = 14$. The contours are the nondimensional spanwise vorticity component ω_z.

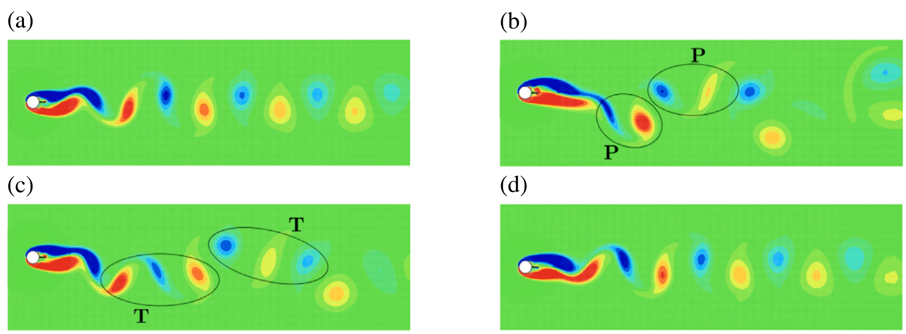

Fig. 12. Vortex shedding modes of the nondimensional splitter plate length $L^* = 0.5$ case at different reduced velocities (V_r): (a) $V_r = 5$, (b) $V_r = 13$, (c) $V_r = 17$ and (d) $V_r = 21$. The contours are the nondimensional spanwise vorticity component ω_z.

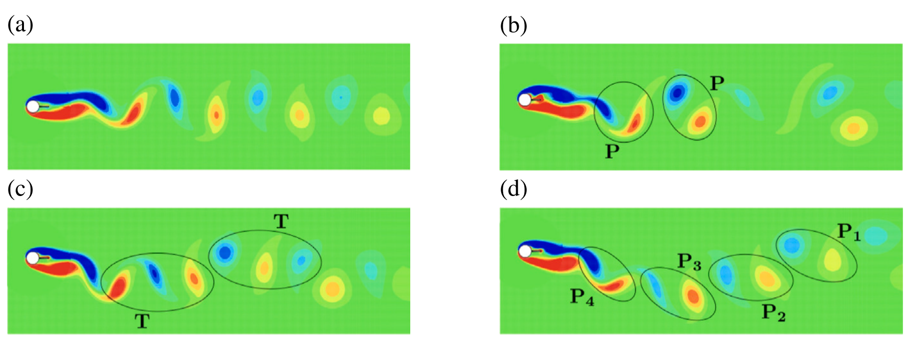

Fig. 13. Vortex shedding modes of the nondimensional splitter plate length $L^* = 0.75$ case at different reduced velocities (V_r): (a) $V_r = 4$, (b) $V_r = 10$, (c) $V_r = 16$ and (d) $V_r = 24$. The contours are the nondimensional spanwise vorticity component ω_z.

vortex shedding mode (two single vortices are shed per vibration cycle) is witnessed at low V_r. The vortices are elongated with the width of the vortex street broadened as V_r is increased to 7. Fig. 11(b) also shows that the shear layers separated from the cylinder surface reattach onto the splitter plate. A 2P vortex shedding mode (two pairs of vortices are shed per vibration cycle) first reported by Brika and Laneville [63,64] is found to be accompanied by shear layer reattachment at $V_r = 11$. It is thought that the lower f_{oy}/f_n in the lock-in range of the cylinder-plate assembly in Fig. 4(b) can be attributed to the reattachment of the shear layers. In the desynchronisation branch, the vortex shedding becomes a 2S mode with one single vortex street. For $L^* = 0.5$ in Fig. 12, similar to the $L^* = 0.25$ case, a single-row vortex street is observed at the onset and in the desynchronisation range of VIV with no evident shear layer reattachment. The shear layers apparently reattach onto the surface of the splitter plate in Fig. 12(b) and (c). The vortex shedding is in a 2P mode at $V_r = 13$. In the transition region of the IB and LB at $V_r = 17$, the wake pattern accords with a 2T mode in which two triplets of vortices are shed per vibration cycle. The 2T vortex shedding mode was observed by Jauvtis and Williamson [65] for the super upper branch of the two-degree-of-freedom (2DOF) VIV of a low-mass-damping cylinder. It has also been reported for the VIV of a circular cylinder [66–68] and for the FIV of prisms with other cross-sectional shapes [69,70].

When the cylinder-plate system with $L^* = 0.75$ is subject to combined VIV-galloping response, a single-row vortex street is found at $V_r = 4$ in Fig. 13(a). The wake pattern at $V_r = 10$ is a 2P mode and it changes to a 2T mode around the kink. The 2P and 2T vortex shedding modes in Fig. 13 are qualitatively similar to those in Fig. 12. The wake mode at $V_r = 24$ in Fig. 12(d) is more complicated than the other three V_r values. It can be seen from this subfigure that four pairs of vortices are formed and shed sequentially from the cylinder-plate assembly in one vibration cycle. This vortex shedding pattern is consequently named as a 4P mode following the convention of Williamson and Roshko [71]. The larger vibration amplitude and lower oscillation frequency of the system in the galloping branch give rise to the multi-vortex wake mode. In Fig. 13, the reattachment of the separated shear layers is found to be associated with the galloping response and it is known to drive the oscillation of the body as discussed by Assi and Bearman [30], Sun et al.

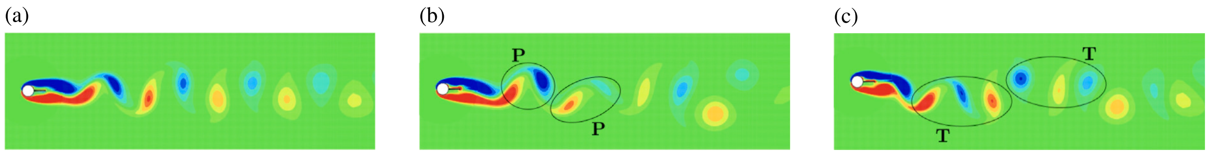

Fig. 14. Vortex shedding modes of the nondimensional splitter plate length $L^* = 1$ case at different reduced velocities (V_r): (a) $V_r = 6$, (b) $V_r = 8$ and (c) $V_r = 14$. The contours are the nondimensional spanwise vorticity component ω_z.

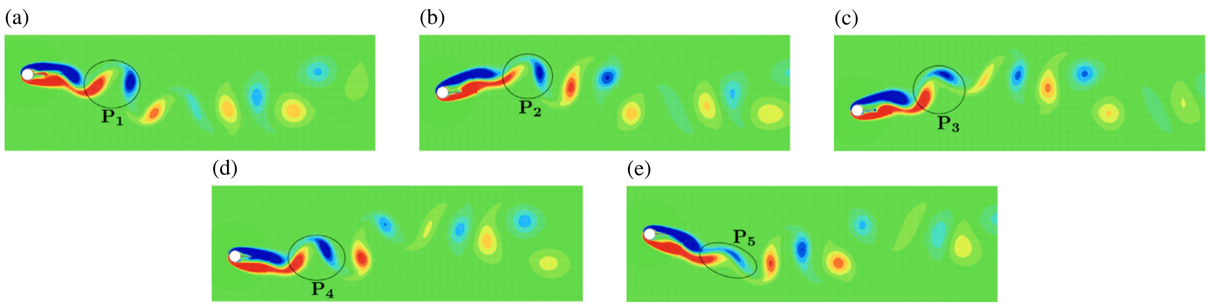

Fig. 15. Vortex evolution of the nondimensional splitter plate length $L^* = 1$ case for the reduced velocity $V_r = 24$ at different time instants in one oscillation cycle: (a) $t = 0T_{oy}$, (b) $t = T_{oy}/5$, (c) $t = 2T_{oy}/5$, (d) $t = 3T_{oy}/5$ and (e) $t = 4T_{oy}/5$. The contours are the nondimensional spanwise vorticity component ω_z.

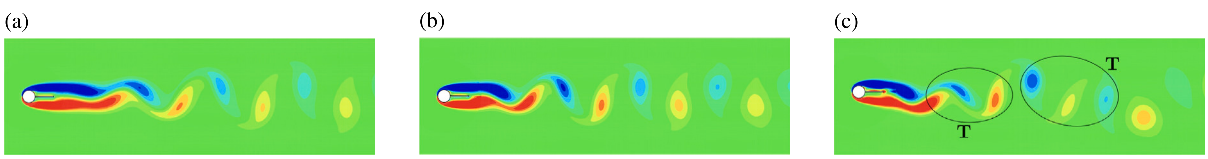

Fig. 16. Vortex shedding modes of the nondimensional splitter plate length $L^* = 1.5$ case at different reduced velocities (V_r): (a) $V_r = 4$, (b) $V_r = 7$ and (c) $V_r = 11$. The contours are the nondimensional spanwise vorticity component ω_z.

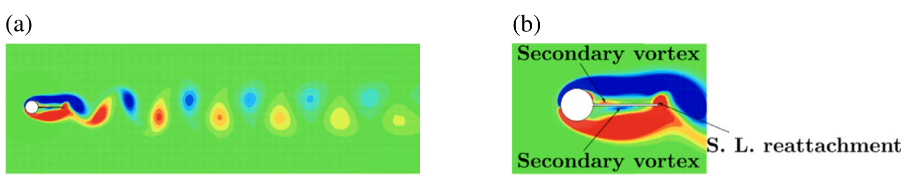

Fig. 17. Vortex shedding mode of the nondimensional splitter plate length $L^* = 2$ case at the reduced velocity $V_r = 4$: (a) wake structure and (b) close-up of the vorticity field around the cylinder-plate assembly. The contours are the nondimensional spanwise vorticity component ω_z.

[24,28]. In terms of the $L^* = 1$ case in Fig. 14, the vortex shedding associated with the VIV peak at $V_r = 6$ is in a 2S mode because of the relatively small A_y/D. At the low end of the galloping branch, the wake pattern changes to a 2P mode at $V_r = 8$ in Fig. 14(b). Similar to the $L^* = 0.75$ configuration, a 2T vortex shedding mode appears around the kink at $V_r = 14$. As for $V_r = 24$, a 5P wake mode is observed with five pairs of vortices shed per oscillation cycle as depicted by the evolution of vortices at different time instants in Fig. 15. When L^* is increased to 1.5, as demonstrated in Fig. 16, the wake patterns in the WVIV region are in a 2S mode. The vortex formation length L_f, represented by the distance from the COG of the cylinder-plate system to the location where the vortices develop and are shed [72–74], becomes smaller with the increase in A_y/D. Unlike the $L^* = 1$ case, the vortex shedding at the onset of the galloping branch changes to a 2T mode. The vortex shedding at the high end of the galloping branch is mostly analogous to the $L^* = 1$ case, i.e., a 5P wake mode. For the largest L^* considered in the present study, the vorticity contours at the VIV peak in Fig. 17 show that apart from the primary vortex shedding in a 2S mode, evident shear layer reattachment is observed at the tip of the splitter plate. Moreover, secondary vortices are formed along the upper and lower surfaces of the splitter plate. The appearance of secondary vortices was also reported by Kwon and Choi [4]. The shear layer reattachment and the secondary vortices are not observed for the VIV peaks in the other two WVIV-galloping scenarios. The appearance of the VIV peak at lower V_r with a larger A_y/D can be possibly attributed to the competitions among the shear layer reattachment, primary and secondary vortex shedding. The vortex shedding at the onset of galloping of the $L^* = 2$ case in Fig. 18 turns out to be a 4P mode with four pairs of vortices shed in each vibration cycle. At the high end of V_r, an additional vortex pair is formed and shed compared to its counterparts in the $L^* = 1$ and 1.5 cases constituting a 6P wake pattern as there are six pairs of vortices shed per oscillation cycle as demonstrated in Fig. 19. A summary of the vortex shedding patterns at different V_r values for each of the L^* considered in this study are provided in Table 3. When $L^* = 0$–0.5 where the system is undergoing pure VIV, the increase in A_y/D with increasing L^* leads to the 2P mode in the UB of $L^* = 0.25$ as well as the 2P and 2T modes in the IB and UB of $L^* = 0.5$. For the combined VIV-galloping and WVIV-galloping responses ($L^* = 0.75$–2), the vortex shedding in the VIV region remains to be the 2S mode. The longer the splitter plate is, the wider the VIV desynchronisation branch becomes and the higher V_r the 2S pattern persists to. The low-frequency but large-amplitude oscillations in the galloping branch give rise to multi-vortex wake patterns. The kink in the galloping response is associated with a switch in the wake modes and more vortices are shed in each vibration cycle with the increase in L^*. A wake mode consists of up to six pairs of vortices in each oscillation cycle is identified within the present parameter space.

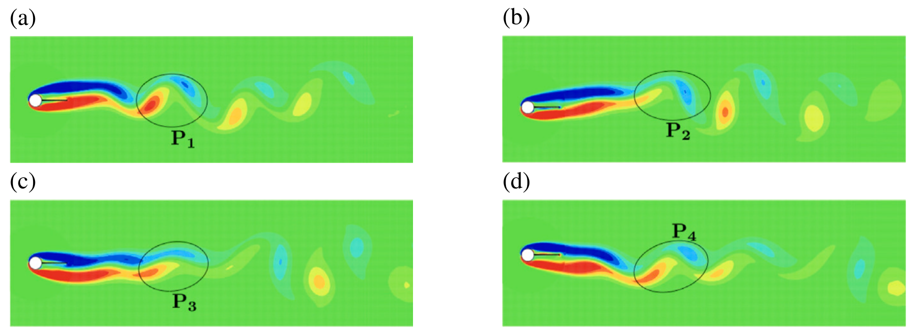

Fig. 18. Vortex evolution of the nondimensional splitter plate length $L^* = 2$ case for the reduced velocity $V_r = 15$ at different time instants in one oscillation cycle: (a) $t = T_{oy}/8$, (b) $t = 3T_{oy}/8$, (c) $t = 5T_{oy}/8$ and (d) $7T_{oy}/8$. The contours are the nondimensional spanwise vorticity component ω_z.

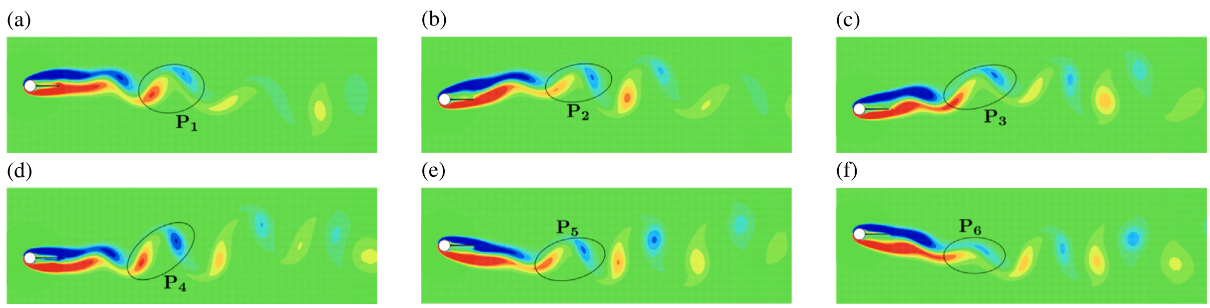

Fig. 19. Vortex evolution of the nondimensional splitter plate length $L^* = 2$ case for the reduced velocity $V_r = 24$ at different time instants in one oscillation cycle: (a) $t = T_{oy}/7$, (b) $t = 2T_{oy}/7$, (c) $t = 3T_{oy}/7$, (d) $9T_{oy}/14$, (e) $11T_{oy}/14$ and (f) $13T_{oy}/14$. The contours are the nondimensional spanwise vorticity component ω_z.

Table 3
Summary of vortex shedding modes in all the cases considered in the present research.

V_r \ L^*	0	0.25	0.5	0.75	1	1.5	2
2	2S	2S	2S	2S	2S	2S	2S
3	2S	2S	2S	2S	2S	2S	2S
4	2S	2S	2S	2S	2S	2S	2S
5	2S	2S	2S	2S	2S	2S	2S
6	2S	2S	2S	2S	2S	2S	2S
7	2S	2S	2S	2S	2S	2S	2S
8	2S	2S	2S	2P	2P	2S	2S
9	2S	2S	2S	2P	2P	2S	2S
10	2S	2P	2P	2P	2P	2S	2S
11	2S	2P	2P	2P	2P	2T	2S
12	2S	2S	2P	2P	2P	2T	2S
13	2S	2S	2P	2P	2T	2T	2S
14	2S	2S	2P	2T	2T	2T	2S
15	2S	2S	2T	2T	2T	2T	4P
16	2S	2S	2T	2T	2T	2T	4P
17	2S	2S	2T	2T	2T	4P	5P
18	2S	2S	2T	2T	2T	4P	5P
19	2S	2S	2S	2T	2T	4P	5P
20	2S	2S	2S	2T	4P	5P	5P
21	2S	2S	2S	2T	4P	5P	5P
22	2S	2S	2S	4P	5P	5P	5P
23	2S	2S	2S	4P	5P	5P	6P
24	2S	2S	2S	4P	5P	5P	6P
25	2S	2S	2S	4P	5P	5P	6P
26	2S	2S	2S	5P	5P	6P	6P

5. Conclusions

The effect of L^* on the FIV of a cylinder-plate assembly with mass ratio $m^* = 10$ and damping ratio $\zeta = 0$ is numerically investigated at $Re = 100$. Seven different L^* values covering the range of 0–2 are considered and V_r is varied systematically from 2 to 26. Important aspects of FIV such as the amplitude and frequency responses, vortex and total phases, hydrodynamic coefficients and wake patterns are analysed. The main conclusions of this paper are as follows:

Three different response patterns are observed, i.e., VIV ($L^* = 0$–0.5), combined VIV-galloping ($L^* = 0.75$) and WVIV-galloping ($L^* = 1$, 1.5 and 2). When the cylinder-plate system is subject to VIV, A_y/D increases and the onset of lock-in is slightly delayed with wider lock-in range as L^* is increased. For combined VIV-galloping and WVIV-galloping, the onset of galloping is associated with a drop in f_{oy}/f_n. A kink attributed to the third harmonic component in F_y is found in the galloping branch which gradually disappears with increasing L^*. In the cases of the VIV response, the transitions from the IB to UB and UB to LB are linked to the jumps in ϕ_{vortex} and ϕ_{total}, respectively. The combined VIV-galloping features $\phi_{vortex} = \phi_{total} = 0°$ throughout the V_r range considered, indicating the direct transition from the IB to galloping branch. Whereas, for the WVIV-galloping response, both ϕ_{vortex} and ϕ_{total} jump to 180° in the LB and fall back to 0° at the onset of galloping. Once the system is undergoing galloping, F_{vortex} and F_y are in phase with y/D.

The peaks of $\overline{C}_x$ and C'_x appear near the low ends of the VIV lock-in regions and their values decrease with increasing L^*. For combined VIV-galloping, $\overline{C}_x$ and C'_x increase with V_r, then experience slight decreases around the kink and eventually remain constant. In terms of WVIV-galloping, the first peaks of $\overline{C}_x$ and C'_x take place in the WVIV regime. They start to increase on the initiation of galloping and reach the plateaus at the kinks. C'_y value becomes higher and the appearance of the peak C'_y value is postponed to higher V_r as L^* is increased. When the system is undergoing VIV, C_{ay} decreases as V_r is increased before the frequency synchronisation and reaches a plateau in the lock-in range. A higher plateau value is found for longer L^* and C_{ay} further reduces in the desynchronisation branch. C_{ay} of the combined VIV-galloping response keeps a decreasing trend. As for the WVIV-galloping pattern, C_{ay} drops significantly in the WVIV region and then leaps at the onset of galloping. Overall, positive C_{ay} is observed in the galloping branch. C_{ey} is mostly negative for the zero-damping system. The troughs of C_{ey} in the VIV cases appear around the low ends of the lock-in ranges. Whereas, they are found to be associated with the kinks in the combined VIV-galloping and WVIV-galloping scenarios.

The wake patterns of the oscillating cylinder-plate assembly are more complicated than those of the plain cylinder. The 2S mode is the most common wake pattern for the VIV response of the system. As L^* is increased, the corresponding increase in A_y/D in the lock-in range brings about the 2P and 2T vortex shedding modes together with the reattachment of the shear layers. For the largest L^* considered, competitions among the shear layer reattachment, primary and secondary vortex shedding are found at the VIV peak. The occurrence of the multi-vortex wake modes in the galloping branch can be attributed to the large-amplitude oscillations at low frequencies. The vortex shedding mode changes in reflection of the kink in the galloping response. It is revealed that the shear layer reattachment phenomenon starts to appear at lower V_r values and the number of vortex pairs in one galloping cycle increases with enlarged L^*. In terms of the future research, more experimental and numerical efforts are necessary to study the effects of m^*, ζ and Re on the FIV characteristics of a cylinder-plate system in detail. The energy conversion characteristics of a cylinder-plate assembly when it is subject to the FIV can also be investigated to assess the feasibility of using such a device to harness the hydrokinetic energy.

CRediT authorship contribution statement

Enhao Wang: Conceptualisation, Methodology, Formal analysis, Supervision, Funding acquisition, Writing – original draft, Writing – review & editing. **Sihan Zhao:** Data curation, Investigation, Validation, Visualisation. **Wanhai Xu:** Data curation, Funding acquisition, Writing – review & editing. **Qing Xiao:** Supervision, Writing – review & editing. **Bing Li:** Writing – review & editing.

Declaration of competing interest

The authors declare that they have no known competing financial interests or personal relationships that could have appeared to influence the work reported in this paper.

Data availability

Data will be made available on request.

Acknowledgements

This research was supported by the National Natural Science Foundation of China [grant numbers 52271282, 51909189 and U2106223], Guangdong Basic and Applied Basic Research Foundation [grant number 2022A1515010846] and Tsinghua Shenzhen International Graduate School via the Scientific Research Start-Up Funds [grant number QD2021023C].

References

[1] Sun Y, Wang J, Fan D, Zheng H, Hu Z. The roles of rigid splitter plates in flow-induced vibration of a circular cylinder. Phys Fluids 2022;34(11):114114.
[2] Apelt CJ, West GS, Szewczyk AA. The effects of wake splitter plates on the flow past a circular cylinder in the range of $10^4 < R < 5 \times 10^4$. J Fluid Mech 1973;61(1):187–98.
[3] Apelt CJ, West GS. The effects of wake splitter plates on bluff-body flow in the range $10^4 < R < 5 \times 10^4$. Part 2. J Fluid Mech 1975;71(1):145–60.
[4] Kwon K, Choi H. Control of laminar vortex shedding behind a circular cylinder using splitter plates. Phys Fluids 1996;8(2):479–86.
[5] Anderson EA, Szewczyk AA. Effects of a splitter plate on the near wake of a circular cylinder in 2 and 3-dimensional flow configurations. Exp Fluids 1997;23(2):161–74.
[6] Deep D, Sahasranaman A, Senthilkumar S. POD analysis of the wake behind a circualr cylinder with splitter plate. Eur J Mech B Fluids 2022;93:1–12.
[7] Hwang JY, Yang KS, Sun SH. Reduction of flow-induced forces on a circular cylinder using a detached splitter plate. Phys Fluids 2003;15(8):2433.
[8] Dehkordi BG, Jafari HH. On the suppression of vortex shedding from circular cylinders using detached short splitter-plates. J Fluid Eng 2010;132(4):044501.
[9] Serson D, Meneghini JR, Carmo BS, Volpe EV, Gioria RS. Wake transition in the flow around a circular cylinder with a splitter plate. J Fluid Mech 2014;755:582–602.
[10] Akilli H, Sahin B, Tumen NF. Suppression of vortex shedding of circular cylinder in shallow water by a splitter plate. Flow Meas Instrum 2005;16(4):211–9.
[11] Cardell GS. Flow past a circular cylinder with a permeable wake splitter plate [Ph.D. thesis], California Institute of Technology; 1993.
[12] Cimbala JM, Garg S. Flow in the wake of a freely rotatable cylinder with splitter plate. AIAA J 1991;29(6):1001–3.
[13] Cimbala JM, Chen KT. Supercritical Reynolds number experiments on a freely rotatble cylinder/splitter plate body. Phys Fluids 1994;6(7):2440–5.
[14] Lu L, Guo X, Tang G, Liu M, Chen C, Xie Z. Numerical investigation of flow-induced rotary oscillation of circular cylinder with rigid splitter plate. Phys Fluids 2016;28(9):093604.
[15] Gu F, Wang JS, Qiao XQ, Huang Z. Pressure distribution, fluctuating forces and vortex shedding behaviour of circular cylinder with rotatable splitter plates. J Fluids Struct 2012;28:263–78.
[16] Sudhakar Y, Vengadesan S. Vortex shedding characteristics of a circular cylinder with an oscillating wake splitter plate. Comput & Fluids 2012;53:40–52.
[17] Every MJ, King R, Weaver DS. Vortex-excited vibrations of cylinders and cables and their suppression. Ocean Eng 1982;9(2):135–57.
[18] Assi GRS, Bearman PW, Kitney N. Low drag solutions for suppressing vortex-induced vibration of circular cylinders. J Fluids Struct 2009;25(4):666–75.
[19] Huera-Huarte FJ. On splitter plate coverage for suppression of vortex-induced vibrations of flexible cylinders. Appl Ocean Res 2014;48:244–9.
[20] Li F, Guo H, Li X, Gu H, Liu R, Zhao C. Experimental investigation on flow-induced vibration control of flexible risers fitted with new configuration of splitter plates. Ocean Eng 2022;266:112597.
[21] Guan G, He K, Wang P, Yang Q. Study on the parameters of detached splitter plate for VIV suppression. Ocean Eng 2022;266:113092.
[22] Stappenbelt B. Splitter-plate wake stabilisation and low aspect ratio cylinder flow-induced vibration mitigation. Int J Offshore Polar Eng 2010;20(3):1–6.
[23] Lou M, Chen Z, Chen P. Experimental investigation of the suppressio of vortex induced vibration of two interfering risers with splitter plates. J Nat Gas Sci Eng 2016;35(A):736–52.
[24] Sun Y, Wang J, Hu Z, Lin K, Fan D. Transition of FIV for a circular cylinder with splitter plates. Int J Mech Sci 2022;227:107429.
[25] Assi GRS, Bearman PW, Tognarelli MA. On the stability of a free-to-rotate short-tail fairing and a splitter plate as suppressors of vortex-induced vibration. Ocean Eng 2014;92:234–44.
[26] Liang S, Wang J, Hu Z. VIV and galloping response of a circular cylinder with rigid detached splitter plates. Ocean Eng 2018;162:176–86.
[27] Zhu H, Li G, Wang J. Flow-induced vibration of a circular cylinder with splitter plates placed upstream and downstream individually and simultaneously. Appl Ocean Res 2020;97:102084.
[28] Sun X, Suh CS, Ye ZH, Yu B. Dynamics of a circular cylinder with an attached splitter plate in larminar flow: A transition from vortex-induced vibration to galloping. Phys Fluids 2020;32(2):027104.
[29] Tang T, Zhu H, Li G, Song J. Comparative study of the flow-induced vibration of a circular cylinder attached with front and/or rear splitter plates at a low Reynolds number of 120. J Offshore Mech Arct Eng 2022;145(1):010904.
[30] Assi GRS, Bearman PW. Transverse galloping of circular cylinders fitted with solid and slotted splitter plates. J Fluids Struct 2015;54:263–80.
[31] Law YZ, Jaiman RK. Wake stabilisation mechanism of low-drag suppression devices for vortex-induced vibration. J Fluids Struct 2017;70:428–49.
[32] Cui GP, Feng LH, Hu YW. Flow-induced vibration control of a circular cylinder by using flexible and rigid splitter plates. Ocean Eng 2022;249:110939.
[33] Issa RI. Solution of the implicitly discretised fluid flow equations by operator-splitting. J Comput Phys 1986;62(1):40–65.
[34] Chan WM, Pandya SA. Advances in distance-based hole cuts on overset grids. In: The 22nd AIAA computational fluid dynamics conference, no. 3425. Dallas, USA, 2015.
[35] Druyor CT. Advances in parallel overset domain assembly [Ph.D. thesis], The University of Tennessee at Chattanooga; 2016.
[36] Chen H, Qian L, Ma Z, Bai W, Li Y, Causon D, Mingham C. Application of an overset mesh based numerical wave tank for modelling realistic free-surface hydrodynamic problems. Ocean Eng 2019;176:97–117.
[37] Newmark NM. A method of computation for structural dynamics. J Eng Mech 1959;85(3):67–94.
[38] Wang E, Xu W, Gao X, Liu L, Xiao Q, Ramesh K. The effect of cubic stiffness nonlinearity on the vortex-induced vibration of a circular cylinder at low Reynolds numbers. Ocean Eng 2019;173:12–27.
[39] Liu Y, Liu F, Wang E, Xiao Q, Li L. The effect of base column on vortex-induced vibration of a circular cylinder with low aspect ratio. Ocean Eng 2020;196:106822.

[40] Leontini JS, Thompson MC, Hourigan K. The beginning of branching behavious of vortex-induced vibration during two-dimensional flow. J Fluids Struct 2006;22(6–7):857–64.
[41] Bao Y, Huang C, Zhou D, Tu J, Han Z. Two-degree-of-freedom flow-induced vibrations on isolated and tandem cylinders with varying natural frequency ratios. J Fluids Struct 2012;35:50–75.
[42] Zhao M, Cheng L, Zhou T. Numerical simulation of vortex-induced vibration of a square cylinder at a low Reynolds number. Phys Fluids 2013;25(2):023603.
[43] Soti AK, De A. Vortex-induced vibrations of a confined circular cylinder for efficient flow power extraction. Phys Fluids 2020;32(3):033603.
[44] VanderPlas JT. Understanding the lomb-scargle periodogram. Astrophys J Suppl Ser 2018;236(1):16.
[45] Terziev M, Tezdogan T, Incecik A. Numerical assessment of the scale effects of a ship advancing through restricted waters. Ocean Eng 2021;229:108972.
[46] Song S, Terziev M, Tezdogan T, Demirel YK, Muscat-Fenech CDM, Incecik A. Investigating roughness effects on ship resistence in shallow waters. Ocean Eng 2023;270:113643.
[47] Wang E, Ramesh K, Killen S, Viola IM. On the nonlinear dynamics of self-sustained limit-cycle oscillations in a flapping-foil energy harvester. J Fluids Struct 2018;83:339–57.
[48] Stern F, Wilson RV, Coleman HW, Paterson EG. Comprehensive approach to verification and validation of CFD simulations–Part 1: Methodology and procedures. J Fluids Eng 2001;123(4):793–802.
[49] Roache PJ. Verification and validation in fluids engineering: Some current issues. J Fluids Eng 2016;138(10):101205.
[50] Bearman PW, Gartshore IE, Maull DJ, Parkinson GV. Experiments on flow-induced vibration of a square-section cylinder. J Fluids Struct 1987;1(1):19–34.
[51] Nemes A, Zhao J, Jacono DL, Sheridan J. The interaction between flow-induced vibration mechanisms of a square cylinder with varying angles of attack. J Fluid Mech 2012;710:102–30.
[52] Bourguet R, Jacono DL. In-line flow-induced vibrations of a rotating cylinder. J Fluid Mech 2015;781:127–65.
[53] Sahu TR, Furquan M, Jaiswal Y, Mittal S. Flow-induced vibration of a circular cylinder with rigid splitter plate. J Fluids Struct 2019;89:244–56.
[54] Zhao J, Hourigan K, Thompson MC. An experimental investigation of flow-induced vibration of high-side-ratio rectangular cylinders. J Fluids Struct 2019;91:102580.
[55] Govardhan R, Williamson CHK. Modes of vortex formation and frequency response of a freely vibrating cylinder. J Fluid Mech 2000;420:85–130.
[56] Song L, Fu S, Cao J, Ma L, Wu J. An investigation into the hydrodynamics of a flexible riser undergoing vortex-induced vibration. J Fluids Struct 2016;63:325–50.
[57] Xu W, Wu H, Jia K, Wang E. Numerical investigation into the effect of spacing on the flow-induced vibrations of two tandem circular cylinders at subcritical Reynolds numbers. Ocean Eng 2021;236:109521.
[58] Lin K, Fan D, Wang J. Dynamic response and hydrodynamic coefficients of a cylinder oscillating in crossflow with an upstream wake interference. Ocean Eng 2020;209:107520.
[59] Wang Z, Fan D, Triantafyllou MS. Illuminating the complex role of the added mass during vortex induced vibration. Phys Fluids 2021;33(8):085120.
[60] Liu B, Zhu H. Secondary lock-in of vortex-induced vibration and energy transfer characteristics of a vibrating cylinder subject to cross buoyancy. Phys Fluids 2021;33(7):073607.
[61] Yin D, Lie H, Baarholm RJ. Prototype Reynolds number VIV tests on a full-scale rigid riser. In: The 36th international conference on ocean, offshore and arctic engineering. OMAE2017-61415, Trondheim, Norway, 2017.
[62] Srinil N, Zanganeh H, Day A. Two-degree-of-freedom VIV of a circular cylinder with variable natural frequency ratio: Experimental and numerical investigations. Ocean Eng 2013;73:179–94.
[63] Brika D, Laneville A. Vortex-induced vibrations of a long flexible circular cylinder. J Fluid Mech 1993;250:481–508.
[64] Brika D, Laneville A. An experimental study of the aeolian vibrations of a flexible circular cylinder at different incidences. J Fluids Struct 1995;9:371–91.
[65] Jauvtis N, Williamson CHK. The effect of two degrees of freedom on vortex-induced vibration at low mass and damping. J Fluid Mech 2004;509:23–62.
[66] Dahl JM, Hover FS, Triantafyllou MS, Dong S, Karniadakis GE. Resonant vibrations of bluff bodies cause multivortex shedding and high frequency forces. Phys Rev Lett 2007;99(14):144503.
[67] Zhao M, Cheng L. Numerical simulation of two-degree-of-freedom vortex-induced vibration of a circular cylinder close to a plane boundary. J Fluids Struct 2011;27(7):1097–110.
[68] Gsell S, Bourguet R, Braza M. Two-degree-of-freedom vortex-induced vibrations of a circular cylinder at $Re = 3900$. J Fluids Struct 2016;67:156–72.
[69] Zhao M. Flow-induced vibrations of square and rectangular cylinders at low Reynolds number. Fluid Dyn Res 2015;47(2):025502.
[70] Seyed-Aghazadeh B, Carlson DW, Modarres-Sadeghi Y. Vortex-induced vibration and galloping of prims with triangular cross-sections. J Fluid Mech 2017;817:590–618.
[71] Williamson CHK, Roshko A. Vortex formation in the wake of an oscillating cylinder. J Fluids Struct 1988;2(4):355–81.
[72] Kovasznay LSG. Hot-wire investigation of the wake behind cylinders at low Reynolds numbers. Proc R Soc Lond Ser A Math Phys Eng Sci 1949;198(1053):174–90.
[73] Roshko A. On the wake and drag of bluff bodies. J Aeronaut Sci 1955;22:124–32.
[74] Green R, Gerrard J. Vorticity measurements in the near wake of a circular cylinder at low Reynolds numbers. J Fluid Mech 1993;246:675–91.